

On-orbit calibration of SeaWiFS

Robert E. Eplee, Jr.,^{1,*} Gerhard Meister,² Frederick S. Patt,¹ Robert A. Barnes,¹
Sean W. Bailey,³ Bryan A. Franz,² and Charles R. McClain²

¹Science Applications International Corporation, 4600 Powdermill Road, Suite 400, Beltsville, Maryland 20705, USA

²Ocean Ecology Branch, Code 616, NASA Goddard Space Flight Center, Greenbelt, Maryland 20771, USA

³FutureTech Corporation, 7307 Hanover Parkway, Suite D, Greenbelt, Maryland 20770, USA

*Corresponding author: Robert.E.Eplee@nasa.gov

Received 25 September 2012; accepted 31 October 2012;
posted 12 November 2012 (Doc. ID 176918); published 20 December 2012

Ocean color climate data records (CDRs) require water-leaving radiances with 5% absolute and 1% relative accuracies as input. Because of the amplification of any sensor calibration errors by the atmospheric correction, the 1% relative accuracy requirement translates into a 0.1% long-term radiometric stability requirement for top-of-the-atmosphere (TOA) radiances. The rigorous prelaunch and on-orbit calibration program developed and implemented for Sea-viewing Wide Field-of-view Sensor (SeaWiFS) by the NASA Ocean Biology Processing Group (OBPG) has led to the incorporation of significant changes into the on-orbit calibration methodology over the 13-year lifetime of the instrument. Evolving instrument performance and ongoing algorithm refinement have resulted in updates to approaches for the lunar, solar, and vicarious calibration of SeaWiFS. The uncertainties in the calibrated TOA radiances are addressed in terms of accuracy (biases in the measurements), precision (scatter in the measurements), and stability (repeatability of the measurements). The biases are 2%–3% from lunar calibration and 1%–2% from vicarious calibration. The precision is 0.16% from solar signal-to-noise ratios, 0.13% from lunar residuals, and 0.10% from vicarious gains. The long-term stability of the TOA radiances, derived from the lunar time series, is 0.13%. The stability of the vicariously calibrated TOA radiances, incorporating the uncertainties of the *in situ* measurements and the atmospheric correction, is 0.30%. This stability of the radiometric calibration of SeaWiFS over its 13-year on-orbit lifetime has allowed the OBPG to produce CDRs from the ocean color data set. © 2012 Optical Society of America

OCIS codes: 280.0280, 010.1690, 120.0280, 120.5630, 280.4788, 280.4991.

1. Introduction

One goal of climate change research is to discern small secular trends in geophysical processes that have comparatively large daily, seasonal, annual, or longer-scale periodic signals. Accordingly, a primary goal of the NASA Ocean Biology Processing Group (OBPG) is to produce a climate data record (CDR) for ocean color data [1]: a time series of measurements of sufficient length, consistency, and continuity that will allow determinations of climate variability and change [2]. This endeavor requires that the remote

sensing data be collected from satellite instruments with long-term radiometric stability, where the radiometric uncertainty in the data is less than the magnitude of the possible climate change signal. For ocean color data, the radiometric requirements are 5% absolute and 1% relative accuracies for the water-leaving radiances [3]. Because ocean surface reflectances are low, approximately 90% of the top-of-the-atmosphere (TOA) signal observed by ocean color satellite instruments arises from scattering of sunlight by gases and aerosols within the atmosphere, as shown in Fig. 1. The ocean color atmospheric correction algorithm must remove the atmospheric signal to yield water-leaving radiances. Due to amplification of errors in the sensor calibration by the

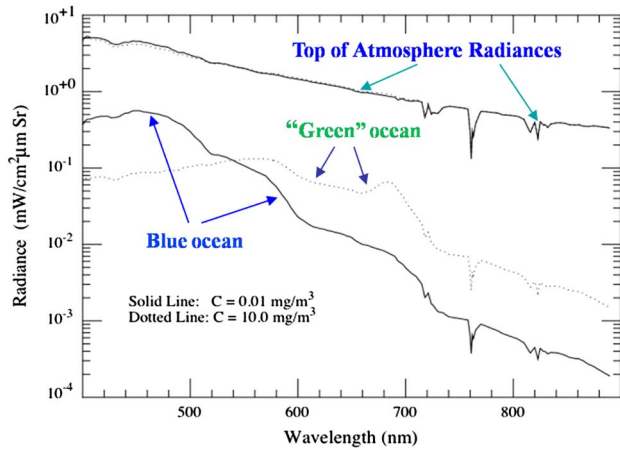


Fig. 1. (Color online) **Ocean color remote sensing.** Spectra are shown for low chlorophyll (blue) and high chlorophyll (green) oceans scenes at the top of the atmosphere and at the ocean surface. Atmospheric correction removes ~90% of the TOA radiance for a given ocean pixel. A calibration error of 0.1% in the TOA radiances introduces an error of 1% in the water-leaving radiances.

atmospheric correction, the 1% relative accuracy requirement on water-leaving radiances translates into a 0.1% long-term radiometric stability requirement for TOA radiances [4]. Uncertainties in the

sensor calibration and atmospheric correction algorithm necessitate a vicarious calibration of the sensor/atmospheric correction algorithm system to meet the accuracy requirements for the TOA radiances [5].

The Sea-viewing Wide Field-of-view Sensor (SeaWiFS) was launched on the OrbView 2 satellite on August 1, 1997 into a polar orbit with a descending node and a nominal node crossing time of local noon. In September 1997 SeaWiFS began providing daily global imagery of the world's oceans in a time series that continued until the satellite ceased communication with the ground in December 2010. The satellite did not have an orbit maintenance capability, so the node of the orbit drifted over time, as shown in Fig. 2. As the orbit node drifted, the scan angle at which SeaWiFS observed the Moon for a given phase angle increased and the β angle of the image of the Sun on the solar diffuser decreased. In 2007 the node drifted later than 1:00 pm and effects of the node drift became discernible in the on-orbit calibration data. These effects will be discussed as necessary in the paper and summarized at the end.

To maximize the long-term stability of the SeaWiFS on-orbit calibration, the OBPB has used monthly lunar calibrations to monitor trends in the instrument response. The Moon provides an

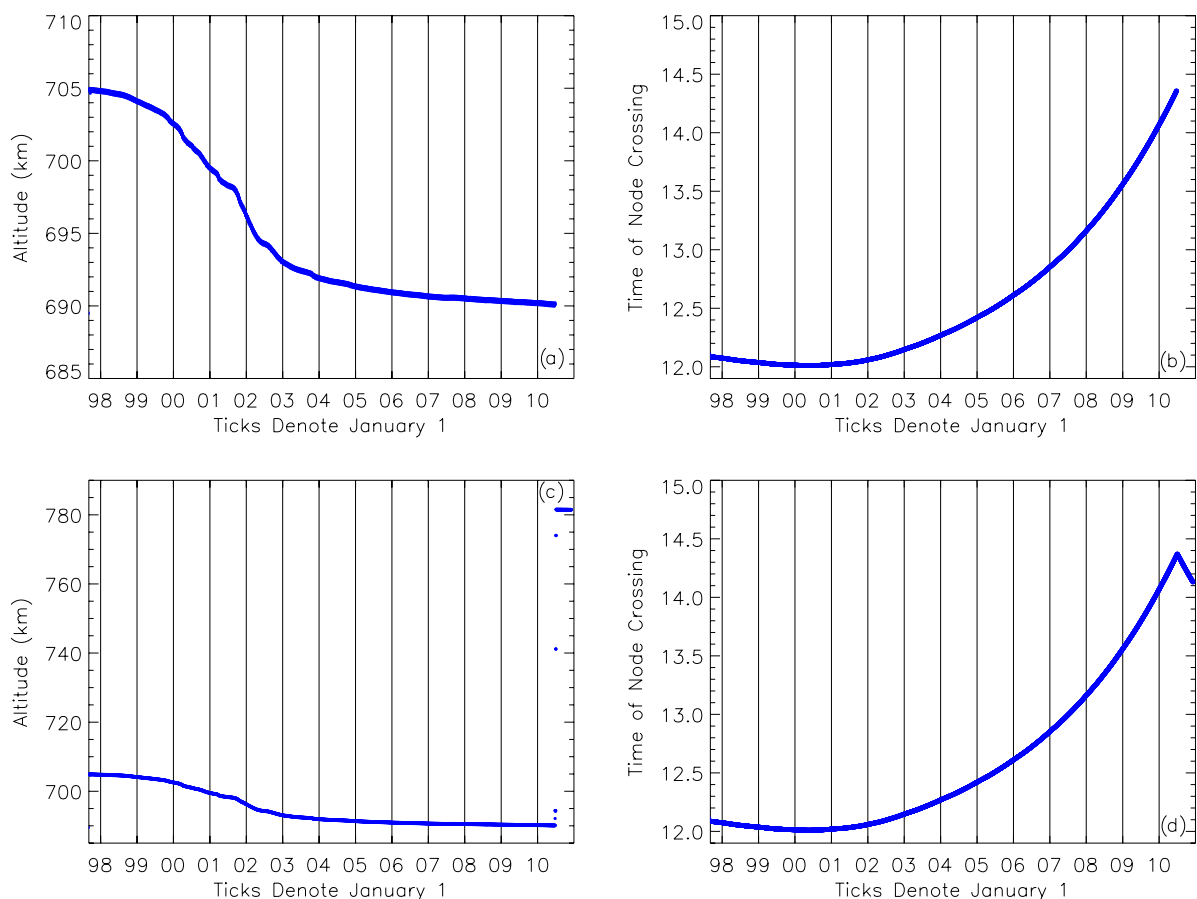


Fig. 2. (Color online) **Orbit node drift.** (a) The spacecraft altitude had decreased from 705 to 690 km between September 1997 and June 2010. (b) The node crossing time had increased from noon to 2:20 pm over this time. (c) The orbit raising maneuver increased the spacecraft altitude from 690 to 782 km. (d) The orbit raising maneuver reversed the direction of the node drift.

Table 1. Lunar Observations^a

Nominal Phase	Phase Angle Range	Number of Observations
-7.0	-6.0 to -8.0	90
+7.0	+5.0 to +10.0	55 (44 ^b)
High	-27.0 to -49.0	27
High	+27.0 to +66.0	32

^a204 lunar observations have been made by SeaWiFS over the period of November 1997–November 2010. 145 observations were obtained at the nominal phase angle of $\pm 7^\circ$ and have been used for long-term radiometric trending. 59 observations were obtained over a range of phase angles and have been used for investigating phase effects in the lunar time series.

^bCals between $+6^\circ$ and $+8^\circ$.

exoatmospheric calibration reference for the reflective solar bands of remote sensing satellite instruments with a long-term stability of 1.0×10^{-8} per year [6]. Over its 13-year lifetime, SeaWiFS collected 145 lunar observations at a nominal phase angle of 7° , distributed before and after full phase, as shown in Table 1. These observations have provided the primary radiometric monitor for the instrument. SeaWiFS collected an additional 59 lunar calibrations at high phase angles for investigation of phase angle effects in the lunar time series. Lunar radiances observed by Earth-orbiting remote sensing instruments depend on the viewing geometry, so over the first 10 years of the mission the OBPG developed a series of analytical and empirical corrections for the variations in the viewing geometry of the lunar data [7]. During the mission the OBPG has also used the lunar calibrations to investigate further aspects of the instrument performance on orbit, particularly radiometric response as a function of focal plane temperature.

Over this time, the US Geological Survey has developed the RObotic Lunar Observatory (ROLO) photometric model of the Moon to provide geometric corrections for on-orbit lunar observations obtained by remote sensing satellite instruments over the wavelength range of 300–2500 nm [8–10]. The model explicitly accounts for the effects of Sun–Moon and instrument–Moon distances and for the effects of phase and libration angles of the lunar observations. The model uses relative spectral responses for each band of a given instrument to generate disk-integrated lunar irradiances as seen by those bands. The OBPG's empirical geometric corrections, when applied to the low phase angle lunar observations, yield a lunar time series that was statistically indistinguishable from the lunar time series processed through the ROLO model [7]. Having validated the performance of the ROLO model over time, though over a limited phase angle range, the OBPG adopted the ROLO model as the primary method for performing geometric corrections for the SeaWiFS lunar data beginning with the SeaWiFS global data reprocessing of July 2007. Use of the ROLO model allows the OBPG to decouple variations in lunar irradiance due

to changes in viewing geometry from variations due to changes in instrument response.

The OBPG's on-orbit calibration strategy also uses daily solar calibrations to monitor short-term changes in instrument response, to monitor the signal-to-noise ratio (SNR) of the instrument on orbit, to monitor changes in the relative reflectance of the two sides of the half-angle mirror, and to monitor the radiometric performance of the individual detectors in each band. The bilinear gain for each band allows long-term radiometric corrections derived from the lunar calibrations for the ensemble of ocean and cloud detectors to be applied to the cloud detectors alone. The detector calibrations validate application of lunar-derived radiometric corrections to cloud-top radiances (allowing stray-light correction of ocean data) and to land radiances (allowing the computation of vegetation indices and surface reflectances).

Since SeaWiFS observes the Moon and the oceans at different instrument gains, the calibration strategy requires that radiometric corrections derived from observations made at one set of gains be applicable to data collected at a different set of gains. Consequently, the strategy uses daily gain calibrations to monitor the temporal stability of the gain ratios for individual detectors in each band.

In order to achieve the calibration accuracy required for the retrievals of water-leaving radiance, the OBPG has vicariously calibrated (VC) the visible bands of SeaWiFS (Bands 1–6) against in-water measurements of the light field made by the Marine Optical BuoY (MOBY) [11,12]. Band 7 (765 nm) been VC relative to Band 8 (865 nm) so that the atmospheric correction algorithm retrieves the expected aerosol types and optical depths for open ocean scenes.

One requirement for producing CDRs from SeaWiFS ocean color data is a quantification of the uncertainties in the calibrated TOA radiances. The error budgets for water-leaving radiances or remote-sensing reflectances begin with the uncertainties in the TOA radiances. The on-orbit calibration data from which these uncertainties can be characterized include lunar observations, solar diffuser observations, gain calibrations, and vicarious calibrations. In this paper, the OBPG will address uncertainties in the calibrated TOA radiances in terms of accuracy (biases in the measurements), stability (repeatability of the measurements over time), and precision (scatter in the measurements). The mean lunar residuals and the vicarious gains provide information on the accuracy of the radiances. The scatter in the lunar residuals, the SNRs determined from solar diffuser measurements, and uncertainties in the vicarious gains provide information on the precision of the radiances. The limits on the residual time drift in the calibrated lunar observations provide information on the long-term stability of the radiances.

Over the mission the performance of SeaWiFS has evolved as the OBPG's understanding of the instrument calibration has steadily increased. At

the same time, the OBPG has continued to refine the algorithms for atmospheric correction, ocean color retrievals, and vicarious calibration. These trends in calibration and algorithms have led the OBPG to implement a series of mission-long global reprocessings of the SeaWiFS data. At each reprocessing, a consistent set of algorithms, an updated instrument calibration, and an updated vicarious calibration are applied to the ocean data from the start of the mission through the forward data processing stream. The updates to the instrument and vicarious calibrations that have been implemented during these data reprocessings are summarized in Table 2.

A. Instrument Background

SeaWiFS is an eight-band visible and near-infrared scanning filter radiometer that is designed to have high radiometric sensitivity over oceans without saturating over bright clouds. The bands are provided in Table 3. Each band is comprised of three high-sensitivity ocean detectors and one low-sensitivity cloud detector. Two bands are arranged on four separate focal planes, where the four detectors from each band are aligned in the along-scan direction and the two bands are located adjacent to each other, as is shown in Fig. 3. For each focal plane, the two outside detectors are the cloud detectors and the interior detectors are the ocean detectors. For normal

Table 3. SeaWiFS Bands^a

Band	1	2	3	4	5	6	7	8
Wavelength	412	443	490	510	555	670	765	865
Bandwidth	20	20	20	20	20	20	40	40

^aThe nominal center wavelengths and bandwidths are in nanometers.

observations, the output from the four detectors in each band are averaged together on orbit, resulting in a bilinear response for the band due to saturation of the ocean detectors at high radiances [13]. This bilinear response can be shown as a calibration curve of radiance as a function of signal from the instrument. The calibration curve for Band 1 at the standard gain is shown in Fig. 4, where the slope of each segment is the counts-to-radiance conversion factor. The point at which each of the ocean detectors saturates is a knee in the bilinear response. The radiances occur below the knee for ocean measurements and above the knee for cloud and land measurements. The bilinear response yields measurements of clouds or land without saturating the band, thus allowing the ocean data to be corrected for stray light, allowing photosynthetically active radiation (PAR) to be computed over the spectral range of 400–700 nm, and allowing land measurements (normalized difference vegetation indexes

Table 2. Calibration Updates for Reprocessing^a

Reprocessing	Date	Calibration Update
R1998.0	January 1998	Use of empirical lunar geometry corrections Prelaunch step function mirror-side corrections Prelaunch temperature corrections Piecewise linear radiometric corrections Forward visible band vicarious calibration at sea surface NIR band vicarious calibration in vicinity of MOBY
R1998.1	August 1998	1st coherent noise correction
R2000.0	May 2000	Updated step-function mirror-side corrections
R2000.1	December 2000	Revised saturated counts for knees of bilinear gains
R2001.0	April 2001	Piecewise quadratic + linear radiometric corrections
R2002.0	July 2002	Piecewise linear mirror-side corrections Revised temperature corrections Exponential radiometric corrections Inverse visible band vicarious calibration at top of atmosphere NIR band vicarious calibration to global open ocean
R2004.0	May 2004	Simultaneous exponential mirror-side corrections
R2005.0	March 2005	Simultaneous exponential radiometric corrections
R2007.0	July 2007	Use of ROLO model for lunar geometry corrections Revised temperature corrections (2 epochs) Piecewise linear Gain 3 drift corrections B7, B8
R2009.0	September 2009	Revised reference temperature (16°C) Prelaunch temperature corrections B1–B5 Revised temperature corrections B6, B7 (1 epoch) Revised temperature corrections B8 (2 epochs) Revised prelaunch counts-to-radiance conversion coefficients Exponential + linear radiometric corrections Quadratic + linear Gain 3 drift correction B7
R2010.0	September 2010	Simultaneous exponential radiometric corrections B1–B2 Exponential + linear radiometric corrections B3–B8

^aChanges to the instrument calibration that were implemented at each reprocessing are shown. For more information on ocean color data reprocessings, see the NASA Ocean Color website: oceancolor.gsfc.nasa.gov/WIKI/OCReproc.html.

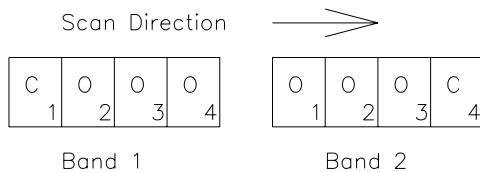


Fig. 3. **Band 1/B and 2 focal plane layout.** The cloud (C) and ocean (O) detectors for each band are laid out on the focal plane as shown.

(NDVI) and surface reflectances) to be made at the radiometric sensitivity of the cloud detectors.

SeaWiFS makes ocean observations at standard instrument gains optimized prior to launch for the expected typical TOA radiances over the oceans in the visible (400–700 nm) and near-infrared (NIR) (700–900 nm) bands. To keep the lunar and solar diffuser measurements below the knee of the bilinear response, the instrument electronics incorporate three additional commanded gains. Gain 2 is a secondary gain for ocean observations (set at 2× the standard gain) designed to maintain the ocean color time series in the event of severe degradation of the radiometric response of a given band, and was never used operationally. Gain 3 is a commanded gain set to give 3/4 full-scale output for lunar observations. Gain 4 is a commanded gain set to give 3/4 full-scale output for solar diffuser measurements. The gain settings for the cloud detectors cannot be changed. After the initial lunar and solar gains were defined the optimum gains for these measurements were recomputed, so the actual commanded gains used on-orbit for ocean, lunar, and solar measurements are shown in Table 4 [14].

SeaWiFS was originally calibrated by the instrument builder, Raytheon Santa Barbara Remote Sensing (SBRS), in November 1993 at the SBRS facility in California during the instrument development [13]. SeaWiFS was recalibrated by the National Institute of Standards and Technology (NIST) in January and April 1997 at Orbital Science Corporation's Germantown, Maryland facility during the integration of the instrument onto the OrbView 2 satellite [15]. The at-launch calibration used by the

Table 4. Commanded Gains^a

Target	Band 1	Band 2	Bands 3–8
Ocean	Gain 1	Gain 1	Gain 1
Lunar	Gain 4	Gain 3	Gain 3
Solar	Gain 3	Gain 1	Gain 3
2×	Gain 2	Gain 2	Gain 2

^aGain 1 is the standard gain for ocean observations. Gain 2 is the secondary gain (2×) for ocean observations. Gain 3 and Gain 4 are the commanded gains designed to give 3/4 full-scale output for lunar and solar observations.

OBPG for processing SeaWiFS data incorporated the focal plane temperature corrections and the response versus scan angle (RVS) corrections from the SBRS calibration and the counts-to-radiance conversion coefficients and the mirror-side reflectance corrections from the NIST calibration.

For a calibrated SeaWiFS observation the total signal is defined as the dark-subtracted counts of the observation, converted to radiance, then corrected for focal plane temperature, RVS, and mirror-side reflectance effects [13,15]:

$$L_T(\lambda, t) = (C_o(\lambda, t) - C_d(\lambda, t))K_c(\lambda)[1 + K_T(\lambda)(T(\lambda, t) - T_{\text{ref}}(\lambda))]K_{\text{rvs}}(\lambda, \text{pxl})K_{\text{ms}}(\lambda, i, t), \quad (1)$$

where

λ	\equiv	SeaWiFS band
t	\equiv	time of the observation
pxl	\equiv	pixel number in the along-scan direction
i	\equiv	Mirror Side 1 or Mirror Side 2
C_o	\equiv	output counts for the observation
C_d	\equiv	dark counts for the observation
K_c	\equiv	counts-to-radiance conversion coefficients
K_T	\equiv	focal plane temperature correction factors
T	\equiv	focal plane temperature for the observation
T_{ref}	\equiv	focal plane reference temperature = 16°C
K_{rvs}	\equiv	RVS correction factors
K_{ms}	\equiv	mirror-side reflectance correction factors

A summary of the uncertainties in the calibration coefficients determined from the prelaunch instrument characterization (K_c , K_{rvs}) and from the

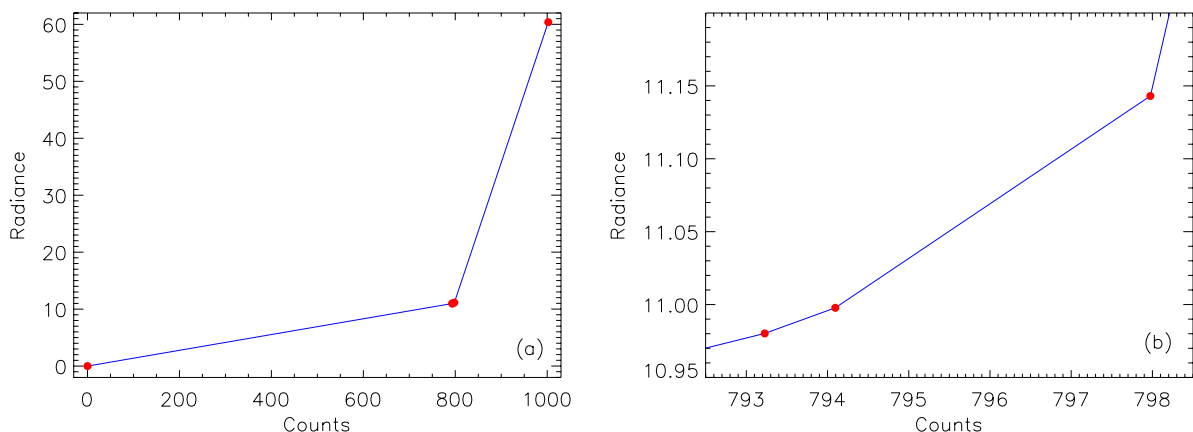


Fig. 4. (Color online) **Calibration curve of Band 1 for the standard gain (Gain 1).** (a) Measurements over the entire dynamic range of the band. (b) Measurements in the vicinity of the knees of the bilinear response. The radiance units are $\text{mW cm}^{-2} \text{sr}^{-1} \mu\text{m}^{-1}$.

Table 5. Instrument Calibration Uncertainties^a

Coefficient		Range (%)	Uncertainty (%)	Applicability
Counts to radiance	K_c		4.0[15]	Calibration bias
Response versus scan angle	K_{rvs}	0.5–1.5	0.3[13]	Precision at end of scan
Focal plane temperature	K_T	0.04–0.09 ^b 0.16–0.27 ^c	0.02	Precision
Mirror side	K_{ms}	0.1	0.01	Precision

^aThe range of values and uncertainties for the parameters are listed, along with the applicability to the uncertainty budget.

^bBands 1–7.

^cBand 8.

detailed on-orbit calibration data analysis (K_T , K_{ms}) are presented in Table 5. Uncertainty in the counts-to-radiance conversion coefficients K_c is the absolute calibration uncertainty and the primary source of the instrument calibration bias. Uncertainty in the RVS correction K_{rvs} is only significant at the end of scan and is smaller than uncertainties in the atmospheric correction at large optical paths. Uncertainty in the focal plane temperature correction K_T is minimized during the lunar data analysis and contributes to the precision estimates. Uncertainty in the mirror-side correction K_{ms} is much smaller than a single instrument count and is essentially negligible.

B. Paper Structure

In this paper, we will examine the on-orbit calibration of SeaWiFS in terms of lunar calibration, focal plane temperature calibration, solar calibration, gain calibration, and vicarious calibration. Each section of the paper will examine the calibration corrections that are computed on orbit, the uncertainties in these corrections, and the uncertainties in the pre-launch instrument characterization, as appropriate. The paper will conclude with the overall uncertainty analysis for the SeaWiFS TOA radiances.

2. Lunar Calibration

SeaWiFS observes the Moon at nadir, which requires a spacecraft pitch maneuver. During this maneuver, the spacecraft is pitched across the Moon so that SeaWiFS views the Moon near nadir through the same optical path as it views the Earth. The spacecraft pitches in the along-track direction at a slower rate than the scan rate of the instrument, resulting in an oversampled image of the Moon. A typical Band 1 lunar image is shown in Fig. 5; the typical lunar image is 8×28 pixels in size. The pitch rate of the spacecraft is not known during a lunar calibration since the spacecraft horizon sensors move off of the Earth, and the rate varies slightly from one pitch maneuver to the next. As a result, the oversampling correction for a given calibration is computed by dividing the actual size of the Moon, as seen from the spacecraft, by the apparent size of the Moon in the lunar image [7]. For each lunar calibration, the observing geometry causes SeaWiFS to view the Moon at a different scan angle; the variation in instrument response with scan angle is corrected by the RVS correction. The ROLO model is used to correct the

lunar observations for viewing geometry (Sun–Moon distance, instrument–Moon distance, phase angle, libration angles).

The lunar calibration time series, corrected for changes in viewing geometry and oversampling, is given by [7]

$$L_{\text{Moon}}(\lambda, t) = L_T(r, \lambda, t)K_{vg}(r, \lambda, t)K_{os}(t)K_{cn}(t), \quad (2)$$

where

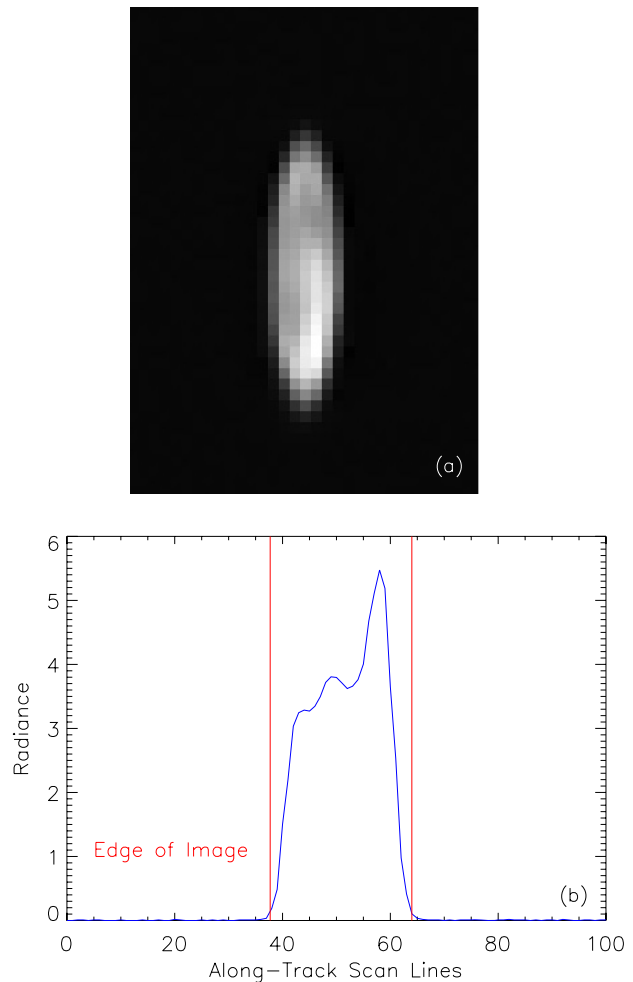


Fig. 5. (Color online) **Band 1 lunar image.** (a) The difference between the spacecraft pitch rate across the Moon and normal pitch rate across the Earth causes the oversampled lunar image. (b) The apparent size of the Moon is derived from the edges in the radiance profile.

K_{vg}	\equiv	corrections for viewing geometry
K_{os}	\equiv	oversampling correction
K_{cn}	\equiv	coherent noise correction

These corrections will be discussed in turn. In practice, the time series is normalized by the first observation so that radiometric trending can occur.

A. Geometric Corrections

The corrections for the viewing geometry of the lunar data, shown in Fig. 6, have the functional form of

$$K_{vg}(r, \lambda, t) = K_d(r, t)K_{ph}(r, \lambda, t)K_{lib}(r, t), \quad (3)$$

where

K_d	\equiv	distance corrections
K_{ph}	\equiv	phase corrections
K_{lib}	\equiv	libration corrections

The distance corrections are given by

$$K_d(r, t) = \left(\frac{R_{\text{Sun-Moon}}(r, t)}{\text{AU}} \right)^2 \left(\frac{R_{\text{Inst-Moon}}(r, t)}{\text{MLD}} \right)^2 \quad (4)$$

where

$R_{\text{Sun-Moon}}$	\equiv	Sun-Moon distance
AU	\equiv	Astronomical unit
$R_{\text{Inst-Moon}}$	\equiv	Instrument-Moon distance
MLD	\equiv	mean Earth-Moon distance = 384401 km

The phase functions of the Moon are defined within the ROLO model by a set of empirically derived polynomials of the phase angle with additional terms arising from the opposition effect [8]. The phase functions for SeaWiFS Bands 1 (412 nm), 5 (555 nm), and 8 (865 nm) are shown in the figure, along with the time series of phase angles for the lunar calibrations. The libration corrections, which are independent of wavelength and account for variations in the selenographic longitude and latitude of the subspacecraft and subsolar points, are also shown in the figure. Since the phase corrections have similar forms over wavelength and since the libration corrections are applied to all the bands, the uncertainties in these corrections are correlated between the bands.

In practice, the ROLO model predicts the reflectances of the Moon based on the phase and libration angles of the observation, computes solar irradiances at one AU for the specified instrument bands, converts the lunar reflectances to irradiances using the solar irradiances, then uses the time of the observation and the position of the spacecraft to normalize the lunar irradiances to the values that should be seen by the instrument. The radiometric output of the model is the residual between the instrument measurement and the model prediction [16]:

$$P(\lambda, t) = \frac{K_d(r, t)}{A_{\text{Moon}}(r, \lambda, t)} \frac{E_{\text{Inst}}(r, \lambda, t)}{E_{\text{Sun}}(\lambda)} - 1 \\ = \frac{E_{\text{Inst}}(r, \lambda, t)}{E_{\text{rolo}}(r, \lambda, t)} - 1, \quad (5)$$

where

A_{Moon}	\equiv	lunar reflectance predicted by the ROLO model
E_{Sun}	\equiv	solar irradiance
E_{rolo}	\equiv	lunar irradiance predicted by the ROLO model

The instrument irradiance is computed from the instrument radiance and the instantaneous field-of-view (IFOV) of SeaWiFS:

$$E_{\text{inst}}(r, \lambda, t) = \text{IFOV}^2 L_T(r, \lambda, t), \quad (6)$$

where $\text{IFOV} \equiv 1.5911$ mrad. The lunar calibration time series derived from the ROLO model, corrected for oversampling and normalized to the first observations so that radiometric trending can occur, is

$$E_{\text{Moon}}(\lambda, t) = \frac{P(\lambda, t) + 1}{P(\lambda, t(0)) + 1} K_{os}(t) K_{cn}(t) \\ = \frac{E_{\text{Inst}}(r, \lambda, t)}{E_{\text{Inst}}(r, \lambda, t(0))} \frac{E_{\text{rolo}}(r, \lambda, t(0))}{E_{\text{rolo}}(r, \lambda, t)} K_{os}(t) K_{cn}(t), \quad (7)$$

where $E_{\text{rolo}} \equiv$ the lunar irradiance predicted by the ROLO model. This lunar irradiance time series is functionally equivalent to the lunar radiance time series given by Eq. (2).

B. Oversampling Correction

As discussed above, the oversampling correction for a given lunar observation is computed by dividing the actual size of the Moon, as seen from the spacecraft, by the apparent size of the Moon in the lunar image. The apparent size of the Moon is derived from edges of the radiance profile across the Moon, as shown in Fig. 5. A detailed discussion of edge determination from the 2nd derivative of the radiance profile is provided by Eplee *et al.* (2004) [7]. The size of the lunar image is dependent on the track angle, the angle between the along-track direction of the spacecraft field-of-view during the pitch maneuver and the rotational axis of the Moon, as shown in Fig. 7. A track that is not along the rotational axis of the Moon could intersect the limb rather than the edge of the Moon, yielding an underestimate of the actual size of the Moon in the image. Such a possible track is shown in the figure. A correction for this underestimation is dependent on both the track angle and the phase angle of the Moon, which determines the location of the terminator. The reduction in the image size due to the phase angle α and the track angle γ is [7]

$$K_{\text{track}}(\alpha, \gamma) = \frac{\cos \alpha}{\sqrt{1 - (1 + \cos \alpha)(1 - \cos \alpha)\cos^2 \gamma}}. \quad (8)$$

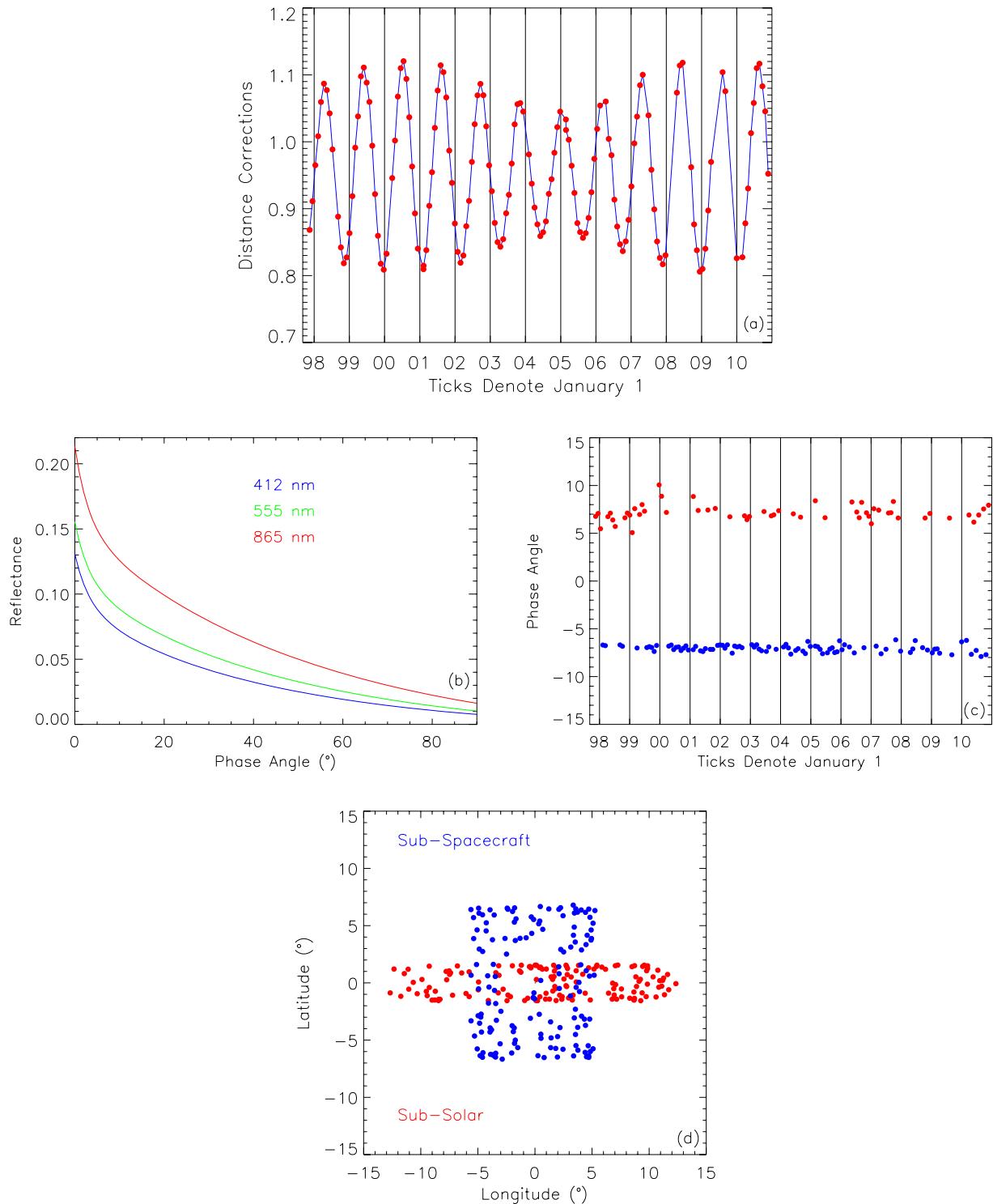


Fig. 6. (Color online) **Lunar geometry corrections.** (a) The Sun–Moon and instrument–Moon distance corrections K_d . (b) The phase function of the Moon at wavelengths of 412, 555, and 865 nm. (c) The time series of phase angles. (d) The libration angles of the subspacecraft and subsolar points.

The size of the Moon, corrected for the track angle, is

$$Y_{\text{Moon}}(\alpha, \gamma, t) = \frac{2}{K_{\text{track}}(\alpha, \gamma) + 1} Y_{\text{obs}}(t), \quad (9)$$

where $Y_{\text{obs}} \equiv$ observed size of the Moon in fractional pixels. The track-angle corrections for the lunar calibration time series have a mean of 1.0013 ± 0.0011 . The corrected size of the Moon is used in computing the oversampling correction for the SeaWiFS lunar images [7,16]:

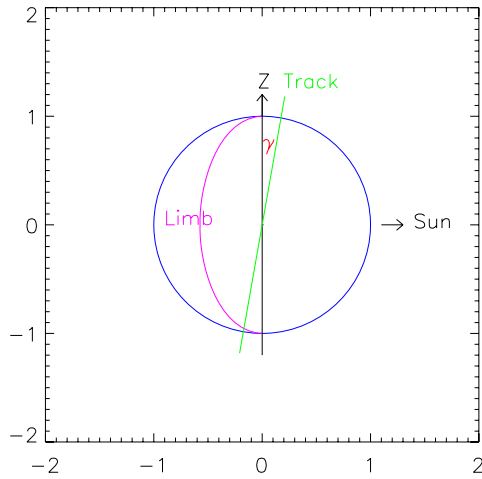


Fig. 7. (Color online) **Spacecraft Track Angle for Lunar Calibrations.** The rotation axis of the Moon is indicated by the vector Z . The spacecraft track across the Moon during a pitch maneuver is indicated by the green line. The angle between the rotation axis and the track is the track angle γ . The lunar disk is illuminated by sunlight coming from the right of the figure. The limb of the illuminated disk is for a phase angle of 55° . The limb for a phase angle of 7° would be indistinguishable from the left edge of the Moon.

$$K_{os}(r, t) = \frac{1}{\theta Y_{Moon}(\alpha, \gamma, t)} \frac{D_{Moon}}{R_{Inst-Moon}(r, t)}, \quad (10)$$

where

$R_{Inst-Moon}$	\equiv	Instrument–Moon distance
θ	\equiv	IFOV of SeaWiFS (1.5911 mrad)
D_{Moon}	\equiv	diameter of the Moon (3476.4 km)

The time series of oversampling correction factors for the lunar calibration time series is shown in Fig. 8. Uncertainties of $\sim 1/4$ pixel in determining the apparent size of the Moon in the lunar images give rise to uncertainties in the oversampling correction of $\sim 2\%$. Since the oversampling correction is applied to all eight bands, the errors in the oversampling correction are correlated between bands. These correlated errors are mitigated by the coherent noise correction discussed in the next section.

C. Coherent Noise Correction

The fully calibrated lunar time series for Bands 1 (412 nm) and 5 (555 nm), as defined by Eq. (7) but without the coherent noise correction applied, are shown in Fig. 9(a). The scatter in the time series arises largely from uncertainties in the oversampling correction, along with contributions from uncertainties in the viewing geometry corrections [16]. The oversampling correction is derived from the determination of the size of the lunar image in the along-track direction, so the $\sim 1/4$ pixel uncertainty in the size of the Moon in a given lunar image results in an $\sim 2\%$ uncertainty in the oversampling correction. Since the same oversampling correction is applied to each band, the errors in the correction are correlated between bands. The coherence in the scatter

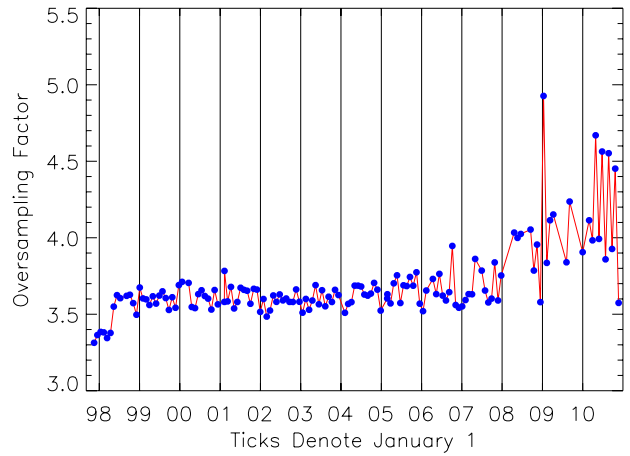


Fig. 8. (Color online) **Lunar oversampling factors.** The time series of oversampling factors. As the orbit node drifts, the scan angle at which SeaWiFS observes the Moon for a given phase angle increases and the track angle of the lunar observation becomes significant. The resulting increase in the uncertainty in the size of the lunar image increases the uncertainty in the oversampling correction. These effects became significant in 2007.

between the two bands is shown by the high correlation between the time series, as plotted in Fig. 9(c). Since Band 5 exhibits the smallest change in radiometric response over time, the OBPB has used this band as the reference band for evaluating noise correlations among all eight bands. Table 6 shows that the noise in the SeaWiFS bands is correlated at the level of 96–99%. The OBPB has used the band-to-band correlation of this noise to implement a coherent noise correction for the lunar time series [7,17].

An estimate of the coherent noise in each band can be determined by computing the residuals of a fit F over time to the lunar time series that does not have the coherent noise correction applied [7]:

$$R_{cn}(\lambda, t) = \frac{E_{Moon}(\lambda, t)K_{os}(t) - F(\lambda, t)}{F(\lambda, t)}. \quad (11)$$

The coherent noise estimates can be contaminated by changes in radiometric response over time, so the OBPB has found that for SeaWiFS the most reliable coherent noise estimates come from the bands that have minimal changes in response with time, Bands 3–5. The high level of correlation in the noise between the SeaWiFS bands has allowed the OBPB to implement a correction to mitigate the coherent noise in the lunar time series:

$$K_{cn}(t) = 1 - \langle R_{cn}(\lambda, t) \rangle_\lambda, \quad (12)$$

where the noise estimates $\langle R_{cn}(\lambda, t) \rangle_\lambda$ are averaged over Bands 3–5. This single coherent noise correction is applied to all eight bands. Table 6 shows that, after the coherent noise correction has been applied, the correlations in the noise between the bands have been reduced by factors of 2–20. The noise correction must not change any time dependence in the

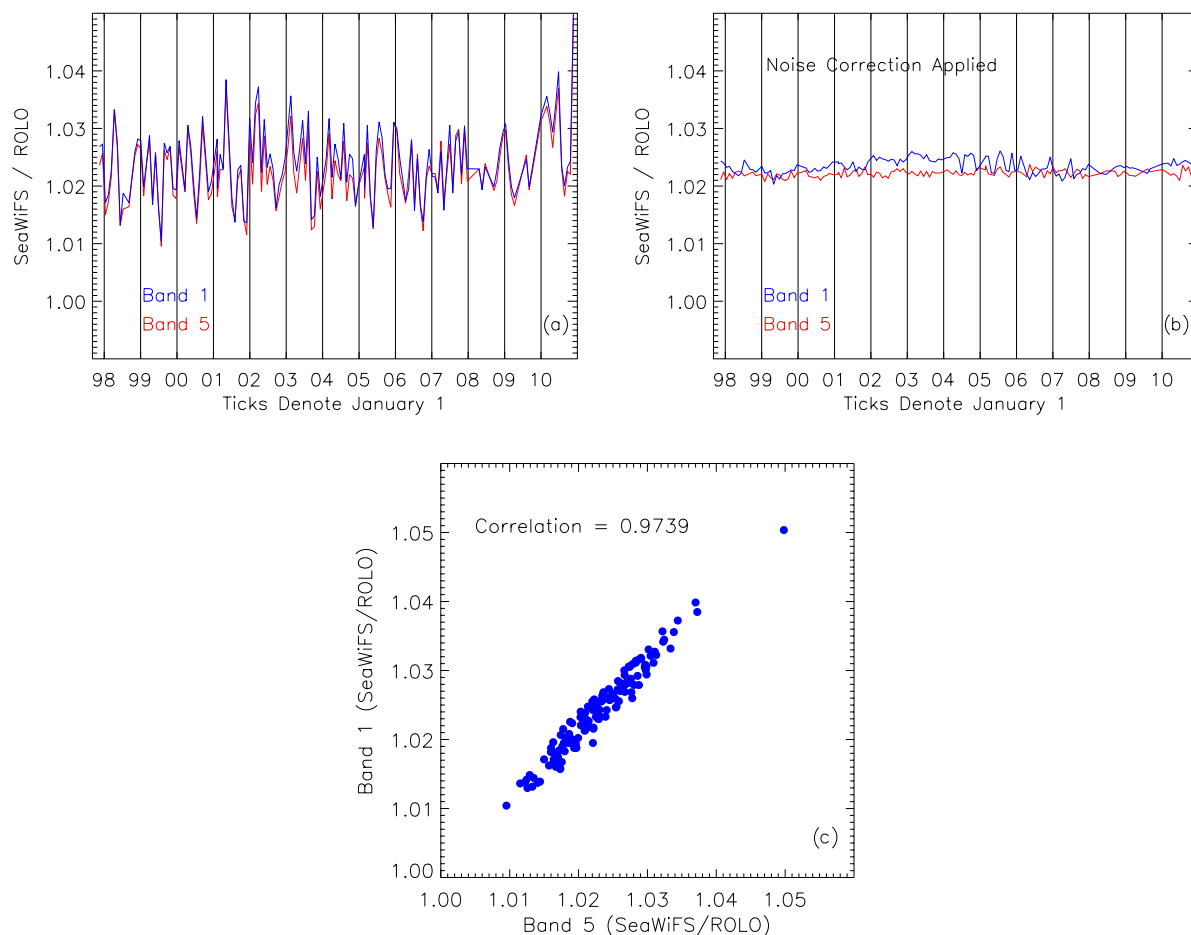


Fig. 9. (Color online) **Correlated Band 1/Band 5 lunar time series.** (a) The time series of fully calibrated lunar observations for Bands 1 and 5 without the coherent noise correction. (b) The time series with the coherent noise correction applied shows the long-term stability of the radiometric calibration of the instrument. (c) The plot of the time series for the two bands shows the correlation of the errors.

radiometric response of the band to which it is applied, so the same fitting function that is used to compute the long-term radiometric correction for the time series is used to compute the noise estimate, an exponential plus linear function or simultaneous exponential functions. For the fully calibrated lunar data with the long-term radiometric correction applied, the fitting function is a linear function time, since any residual radiometric drift in a given band should be small. Figure 9(b) shows Bands 1 and 5 with the coherent noise correction applied. The

residual time dependence for each of the bands is the same with or without the noise correction, which verifies the time independence of the noise correction.

Since the viewing geometry corrections and the oversampling correction only apply to the lunar data, the coherent noise correction K_{cn} mitigates the systematic errors found in K_{vg} and K_{os} , thus minimizing the systematic errors in the long-term radiometric correction K_{rc} that are applied to the Earth data. By doing so, the coherent noise correction allows the uncertainties derived for the lunar time series (with the coherent noise correction) to be applied to the Earth data that is calibrated with the radiometric correction.

D. Functional Form of the Radiometric Fits

The lunar time series (with viewing geometry corrections, oversampling corrections, and coherent noise corrections applied) are shown in Fig. 10. Two different decay mechanisms are responsible for changes in the radiometric response for the bands. The first mechanism caused a rapid change in response that decayed away after the initial couple of years of the mission; there is no current candidate for this

Table 6. Correlated Fully Calibrated Lunar Time Series^a

Bands	λ (nm)	Correlation ^b	Correlation ^c
1/5	412/555	0.9739	0.03447
2/5	443/555	0.9844	0.04884
3/5	490/555	0.9900	0.5510
4/5	510/555	0.9861	0.6714
6/5	670/555	0.9895	0.5258
7/5	765/555	0.9776	0.1678
8/5	865/555	0.9667	0.08396

^aThe correlation between Band 5 and the remaining bands.

^bbefore and

^cafter the coherent noise correction.

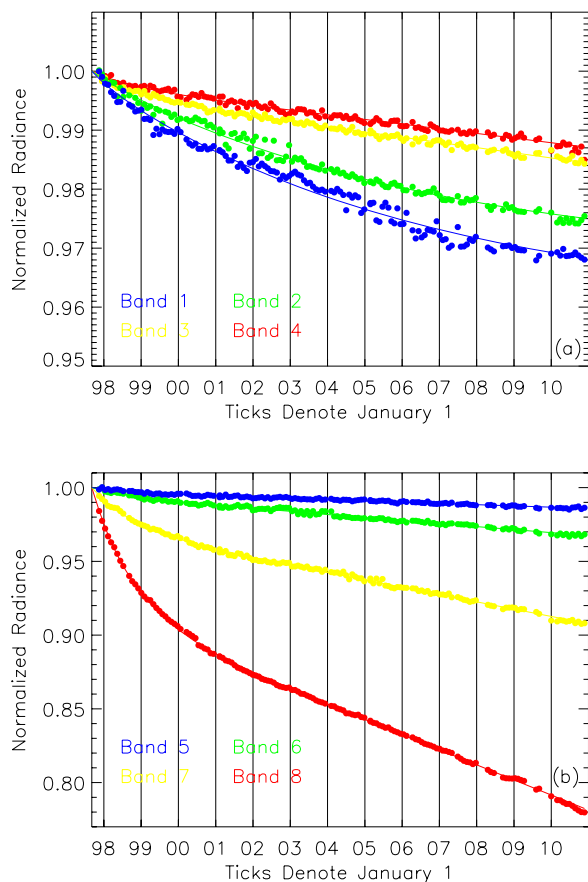


Fig. 10. (Color online) **Lunar Calibration Time Series.** (a) The lunar time series for Bands 1–4, along with long-term radiometric fits. (b) The time series for Bands 5–8, along with long-term radiometric fits.

short-term mechanism. The second mechanism has been in effect over the entire mission; there are two different long-term response degradation processes occurring for SeaWiFS. The shorter wavelength bands (Bands 1–4) show a degradation that decreases with increasing wavelength and is most likely caused by yellowing of the instrument optics on orbit. The longer wavelength bands (Bands 5–8) show a degradation that increases with increasing wavelength and is most likely caused by charged-particle-induced damage to the silicon photodiodes [18]. As the plots show, the degradation over the mission is ~1% for Bands 3–5, is ~3% for Bands 1, 2, and 6, is ~9% for Band 7, and is ~21% for Band 8.

With the short-term and long-term decay mechanisms at work, the OBPG has used different functions for the radiometric fits over the SeaWiFS mission, as shown in Table 2 [19]. At the end of the mission, the optimum fitting functions for the time series are either simultaneous exponentials in time (with short-period and long-period time constants) or are single exponentials (with short-period time constants) plus linear functions of time. The fits to these time series track the long-term radiometric instrument response for each band, so the inverses of the fits are the long-term radiometric corrections K_{rc} :

$$\frac{1}{K_{rc}(\lambda_{1,2}, t)} = A_0(\lambda) - A_1(\lambda)[1 - e^{-\tau_1(\lambda)(t-t_0)}] - A_2(\lambda)[1 - e^{-\tau_2(\lambda)(t-t_0)}] \quad (13)$$

$$\frac{1}{K_{rc}(\lambda_{3-8}, t)} = A_0(\lambda) - A_1(\lambda)[1 - e^{-\tau(\lambda)(t-t_0)}] - A_2(\lambda)(t - t_0), \quad (14)$$

where

A_i	\equiv	fitted values of the function
τ_i	\equiv	time constants of the exponential functions
t_0	\equiv	reference time for the time series

For Bands 1 and 2, the OBPG used a simultaneous exponential with a short-period time constant of 200 days and a long-period time constant of 3200 days to fit the radiometric response of the instrument [using Eq. (2)]. For Bands 3–8, the OBPG used the 400-day exponential plus linear function of time [using Eq. (3)]. The calibration lookup tables incorporate the coefficients A_i and the time constants τ_i of the fitting functions.

The fully calibrated lunar data have the long-term radiometric corrections applied and, ideally, should be constant over time:

$$L_{Moon}(\lambda, t) = L_T(\lambda, t)K_{rc}(\lambda, t)K_{vg}(\lambda, t)K_{os}(t), \quad (15)$$

$$L_{Moon}(\lambda, t) = L_T(\lambda, t)K_{rc}(\lambda, t)K_{vg}(\lambda, t)K_{os}(t)K_{cn}(t), \quad (16)$$

where Eq. (16) has the coherent noise correction applied and where

K_{rc}	\equiv	long-term radiometric correction
K_{vg}	\equiv	viewing geometry correction
K_{os}	\equiv	oversampling correction
K_{cn}	\equiv	coherent noise correction

The time series including the coherent noise correction are shown in Fig. 11. The measured uncertainties in L_{Moon} arise from the root mean square (RMS) error in the radiances and from the calibration biases. The uncertainties from the lunar calibration time series that are applicable to Earth observations are those due to the long-term radiometric correction. Hence, the OBPG minimizes the systematic errors in the lunar observations that are not present in the Earth observations, namely the uncertainties from the oversampling corrections and the viewing geometry corrections, through the coherent noise correction.

E. Validation of the Geometric Corrections

SeaWiFS was launched before the ROLO model was fully operational, so the OBPG developed a set of empirical corrections for phase and libration effects in the lunar calibration time series [7]. These corrections were derived for the limited phase angle range of the low phase lunar calibrations (5°–10°). The libration

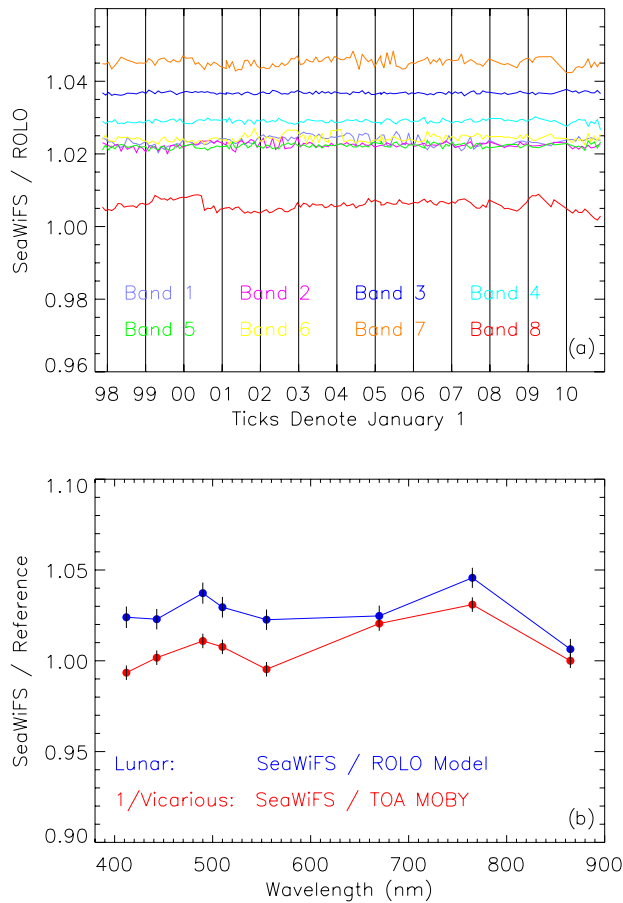


Fig. 11. (Color online) **SeaWiFS on-Orbit Calibrations.** (a) The fully calibrated lunar residuals show the long-term stability of the on-orbit calibration for each band. (b) The mission-averaged lunar residuals from the ROLO model (shown in blue) and the vicarious calibration against MOBY (shown in red) are plotted as functions of wavelength. The error bars for the lunar data are the RMS errors of the time series and the error bars for the vicarious gains are the uncertainties in the gains of 0.001.

corrections were sensitive to changes in the radiometric response of the instrument, so they were derived from Bands 3–5, where the radiometric changes were minimal, and then applied to all eight bands. After the ROLO model had been validated with these empirical corrections, the OBPG incorporated the ROLO model into the SeaWiFS lunar data processing scheme to decouple the geometric corrections from the radiometric response of the instrument and to geometrically correct the high phase angle data [7].

As a final validation of SeaWiFS geometric corrections, the OBPG has recomputed the SeaWiFS empirical geometric corrections for the entire SeaWiFS mission, restricting the dataset to the low phase angle observations around $\pm 7^\circ$. This test used the fully calibrated SeaWiFS lunar radiances (Fig. 11) to eliminate the effects of changing radiometric response on the outcome of the comparison. The test used two versions of the input data, without and with the coherent noise correction applied, to evaluate the effect of the noise correction on the outcome of the comparison.

For the SeaWiFS geometry corrections the OBPG first corrected for the Sun–Moon and instrument–Moon distances and for the oversampling factors. The distance corrections and the oversampling corrections applied here are the same as those implemented in the ROLO model. For the empirical phase corrections the OBPG computed a quadratic fit for each band as a function of phase angle (using before and after full phase datasets) to derive an empirical phase correction. Computing separate corrections before and after full phase is one difference from the past SeaWiFS corrections [7]. For the empirical libration corrections the OBPG performed a regression of the libration angles against the phase-corrected lunar time series for Bands 3–5, computing a mean libration correction, which was then applied to all eight bands, as had been done previously [7].

The radiances for each band after the two types of geometric corrections have been applied agree at the 0.13% level for the time series with the coherent noise correction and at the 0.19% level for the time series without the coherent noise correction. The differences in the two types of geometric corrections are offset by the coherent noise correction, which is not surprising since distance corrections and the libration corrections are independent of wavelength. These differences are comparable in size to the precision of the lunar calibration measurements, as will be discussed in Section 7 of this paper. So over the limited range of phase angles of the SeaWiFS low-phase lunar calibrations, the phase and libration corrections applied by the ROLO model and by the empirical approach are consistent to within the uncertainty of the measurements. These results validate the ROLO geometric corrections for the SeaWiFS low-phase lunar calibrations over the mission, confirming the initial validation of the geometric corrections done for Reprocessing 2007.0 [7].

Use of the ROLO model for the geometric correction of the SeaWiFS lunar calibration time series has allowed the OBPG to decouple variations in lunar irradiance due to changes in viewing geometry from variations due to changes in instrument response. This geometric correction capability has been critical to the OBPG in performing the focal plane temperature calibration of SeaWiFS, as is discussed in the next section of the paper.

3. Focal Plane Temperature Calibration

Over the SeaWiFS mission the OBPG has used lunar calibrations to investigate further aspects of instrument performance on orbit, particularly radiometric response as a function of focal plane temperature. These investigations looked at the focal plane reference temperature and at the focal plane temperature correction coefficients.

A. Focal Plane Reference Temperature

The reference temperature used for the focal plane temperature corrections [T_{ref} from Eq. (1)] for all bands was set at 20°C during the prelaunch characterization

of SeaWiFS [13]. The temperatures for the Band 7/8 focal plane measured on orbit over the mission are shown in Fig. 12. The first plot shows the temperatures measured during lunar calibrations, while the second plot shows the orbit-averaged temperatures measured during the normal collection of ocean data. For both plots, the initial reference temperature is shown in green (upper line). The time series show the seasonal variations in focal plane temperatures due to variations in the Earth–Sun distance. The 4° annual cycle occurs because SeaWiFS does not have a focal plane temperature control system such as those on MODIS or VIIRS. The long-term downward trend in the temperatures likely arises from drift in the orbit node away from local noon.

For both datasets (lunar and ocean) the initial reference temperature is above the normal range of focal plane temperatures experienced by SeaWiFS on orbit. Comparison of the two time series led the

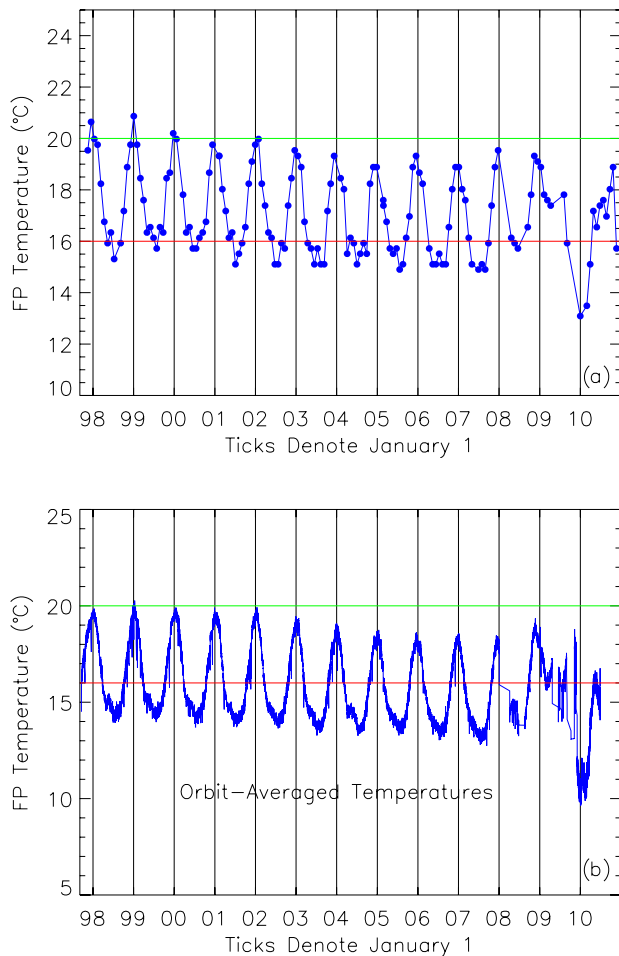


Fig. 12. (Color online) **Band 7/8 Focal Plane Temperatures.** (a) Temperatures during lunar calibrations. (b) Orbit-averaged temperatures for the ocean color dataset. The initial reference temperature of 20°C is shown in green (upper horizontal line) and the revised reference temperature of 16°C is shown in red (lower horizontal line). The changing thermal environment of the spacecraft as a result of the orbit node drift gives rise to the trend in these plots.

OBPG to change the focal plane reference temperature to 16°C for Reprocessing R2009.0 (Table 2). The revised reference temperature is shown in red (lower line) in the two plots. The choice of reference temperature is somewhat arbitrary, but the OBPG chose a temperature that is within the annual temperature variations of both the lunar and ocean datasets.

Changing the reference temperature for an instrument calibration requires adjustment of the counts-to-radiance conversion coefficients [$K_c(\lambda)$ from Eq. (1)] for the calibration to yield the same radiometric gain for a given TOA radiance. For this purpose, the OBPG has defined an effective instrument gain for a given band as follows:

$$G_{\text{eff}}(\lambda, T) = K_c(\lambda)(1 + K_T(\lambda)(T - T_{\text{ref}})). \quad (17)$$

For changes in the temperature correction coefficients and/or the reference temperature, this equation can be used to derive the adjustments in the counts-to-radiance conversion coefficients required to maintain a constant effective gain:

$$\frac{K_c^n(\lambda)}{K_c^o(\lambda)} = \frac{1}{1 + K_T(\lambda)(T_{\text{ref}}^o - T_{\text{ref}}^n)}, \quad (18)$$

where the superscript o denotes the original coefficients and reference temperatures and the superscript n denotes the revised coefficients and reference temperatures. For the eight SeaWiFS bands, the adjustments to the counts-to-radiance conversion coefficients are given in Table 7. The adjustments for Bands 1–7 are small and are compensated for by the vicarious calibration of the instrument. For Band 8, which is not VC, the adjustment is significant (~0.7%). The vicarious calibration does mitigate changes in the Band 8 gain through the assumption that the band retrieves the same aerosol radiances when observing the same open ocean scenes [16]. The counts-to-radiance conversion coefficients incorporated into the calibration lookup table for Reprocessing R2009.0 have had these adjustments applied.

B. Focal Plane Temperature Corrections

The four SeaWiFS focal planes (for Bands 1/2, 3/4, 5/6, and 7/8) result in four focal plane temperatures for the instrument. At the same time, each band has its own focal plane temperature dependence, so there are eight focal plane temperature corrections

Table 7. Counts-to-Radiance Conversion Coefficient Adjustments for Reference Temperature Change

Band	λ (nm)	Adjustment (%)
1	412	0.3627
2	443	0.2335
3	490	0.1677
4	510	0.1558
5	555	0.1562
6	670	−0.01206
7	765	−0.2131
8	865	−0.6583

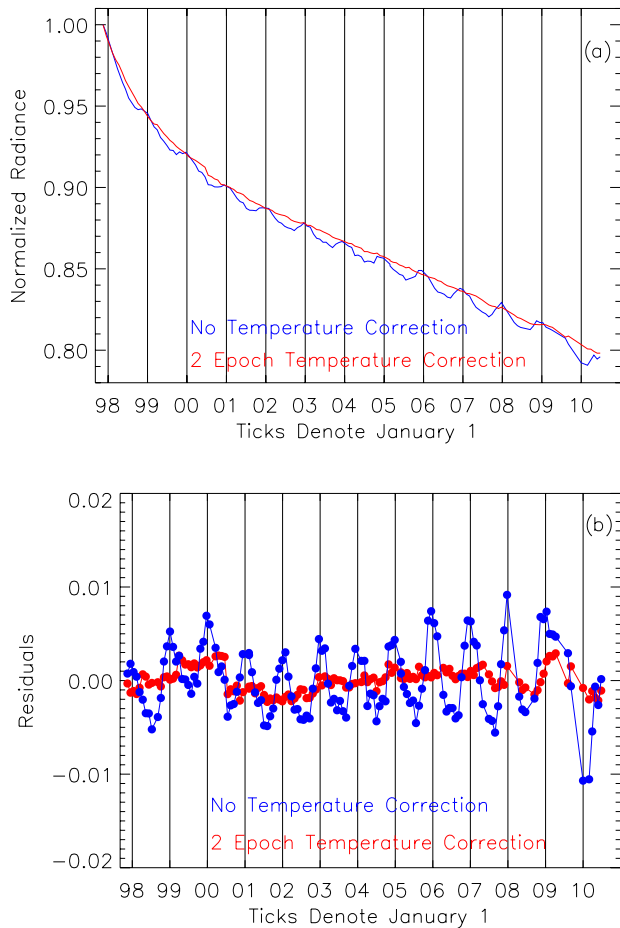


Fig. 13. (Color online) **Band 8 Lunar Temperature Corrections.** The lunar calibration (a) time series and (b) residuals without (blue, with periodicities) and with (red, without periodicities) the focal plane temperature corrections applied.

in the instrument calibration. The temperatures for the Band 7/8 focal plane measured during lunar calibrations over the mission are shown in Fig. 12. To show the dependencies of the radiometric response of Band 8 on the focal plane temperatures, the lunar calibration time series for Band 8 has been processed without and with having the focal plane temperature corrections applied, as shown in Fig. 13(a). Subtraction of the long-term radiometric trend yields the residuals shown in Fig. 13(b).

The dependence of the radiometric response of the SeaWiFS bands on focal plane temperature was originally determined during the 1993 SBRs calibration of SeaWiFS [13]. The resulting focal plane temperature correction has the form

$$K_{TC}(\lambda, T) = 1.0 + K_T(\lambda)(T - T_{ref}), \quad (19)$$

where

K_T	\equiv	temperature correction coefficient
T	\equiv	focal plane temperature
T_{ref}	\equiv	focal plane reference temperature

The prelaunch temperature correction coefficients are shown in Table 8. After launch, the OBPB observed periodic residuals in the lunar calibration time series that were correlated with focal plane temperatures; these residuals were similar to those shown in Fig. 13, though of a smaller magnitude. Through SeaWiFS Reprocessing R2001.0 the OBPB handled these periodicities by a series of piecewise linear and quadratic radiometric corrections that were incorporated into the calibration lookup tables [17,20].

For Reprocessing R2002.0, the OBPB began an evaluation of the focal plane temperature dependence by regressing the focal plane temperatures against lunar calibration residuals derived from data uncorrected for focal plane temperature. The OBPB used a lunar time series of 28 observations (collected through March 2000) to compute a revised set of focal plane temperature correction coefficients that were incorporated into the calibration lookup table for Reprocessing R2002.0 [17,20]. This revision of the coefficients, shown in Table 8, removed the annual periodicities observed in the lunar time series, particularly for Bands 7 and 8.

By mid-2005, annual periodicities in the lunar time series had reappeared in Bands 7 and 8. Consequently, the OBPB generated a second revision of the focal plane temperature corrections based on 114 lunar calibrations (collected through May 2007) that were incorporated into the calibration lookup table for Reprocessing R2007.0 [21] and are shown in Table 8. For the focal plane temperature analyses leading up to Reprocessing R2007.0, the instrument model used in deriving the corrections attributed

Table 8. Focal Plane Temperature Correction Coefficients^a

Band	Prelaunch	First On-Orbit	Second On-Orbit		Current On-Orbit	
			1 Aug 1997	27 Oct 2005	1 Aug 1997	19 Jun 2005
412	0.000910	0.0007664	0.0006635	0.0005259	Prelaunch	same
443	0.000585	0.0005540	0.0004831	0.0004879	Prelaunch	same
490	0.000420	0.0003392	0.0003001	0.0001143	Prelaunch	same
510	0.000390	0.0003057	0.0003035	0.0001688	Prelaunch	same
555	0.000391	0.0003045	0.0003476	0.0001890	Prelaunch	same
670	0.000151	-0.00003443	-0.0006651	-0.0002336	-0.00003015	same
765	0.000106	-0.0004495	-0.0003781	-0.0009472	-0.0005316	same
865	0.000078	-0.001485	-0.001540	-0.002994	-0.001635	-0.002653

^aThe first on-orbit coefficients were introduced with Reprocessing R2002.0, the second on-orbit coefficients were introduced with Reprocessing 2007.0, and the current on-orbit coefficients were introduced with Reprocessing R2009.0. The units are (C°)⁻¹.

the lunar residuals to the temperature response only. This assumption leads to possible biases in the temperature correction coefficients due to any residual changes in the radiometric response of the instrument over time that were not removed by the long-term radiometric corrections.

To avoid such radiometric biases, the OBPG updated the instrument model used in deriving the temperature correction coefficients for Reprocessing R2009.0 to simultaneously solve for the long-term radiometric response of the instrument and for the dependence of the response on focal plane temperatures. The fitting function for the long-term radiometric trend is short-period exponential plus linear function of time, so the function used in the simultaneous regression fits for the long-term radiometric trend and the focal temperature corrections has the form

$$F(\lambda, t, T) = A_0(\lambda) - A_1(\lambda)[1 - e^{-\tau(\lambda)(t-t_0)}] - A_2(\lambda)(t - t_0) - A_3(\lambda)(T(t) - T_{\text{ref}}). \quad (20)$$

Once the optimum focal plane temperature correction coefficients were computed for each band, these coefficients were incorporated in the calibration lookup table and the optimum long-term radiometric corrections were rederived. The OBPG used a lunar time series of 129 observations (collected through January 2009) in this analysis.

The full focal plane temperature dependence analysis for Reprocessing R2009.0 has involved the evaluation of lunar residuals derived three ways:

- (1) without any temperature corrections;
- (2) using the 1993 SBRS prelaunch temperature corrections; and
- (3) using the temperature corrections derived simultaneously with the radiometric corrections using Eq. (20).

The focal plane temperature correction coefficients derived for Bands 1–5 are small relative to those for Bands 6–8. The coefficients for Bands 1–5 yielded lunar residuals that were indistinguishable from the residuals derived using the prelaunch focal plane temperature corrections, so the OBPG has reverted the focal plane temperature corrections K_T for these bands to their prelaunch measured values [13]. The focal plane temperature correction coefficients derived for Bands 6–8 differ from the prelaunch values—there are sign changes in the coefficients and the values for Bands 7 and 8 are larger than the prelaunch values. The lunar residuals for Bands 6 and 7 show correlations with focal plane temperature that warrant using a single temperature correction coefficient derived for each band from the lunar data. The lunar residuals for Band 8 show a change in the focal plane temperature dependence over the mission, warranting the use of two temperature corrections for this band, with the temperature correction epoch boundary in mid-2005. The lunar times series

for Band 8, with the revised focal plane temperature corrections applied, is shown in Fig. 13. The focal plane temperature correction coefficients that have been incorporated into the calibration lookup table for Reprocessing R2009.0 are shown in Table 8 and are valid through the end of the mission.

The uncertainty in the focal plane temperature correction coefficients contributes to the precision of the TOA radiances. The OBPG has minimized this uncertainty during the lunar data analysis used in deriving the coefficients. This analysis shows that the uncertainty in the current (and final) set of focal plane temperature coefficients is 0.02%, as is summarized in Table 5.

4. Solar Calibration

The SeaWiFS daily solar calibrations allow the OBPG to look for short-term changes in the instrument response, to measure the SNRs of the SeaWiFS bands on orbit, to monitor the mirror-side reflectance corrections, and to monitor the radiometric performance of the individual detectors. These different analyses will be examined in turn.

The solar calibration time series for Band 1 is shown in Fig. 14. The orbit node of the Orbview 2 satellite drifted over the mission, giving rise to a temporal trend in the solar β angle. Since the bidirectional reflectance distribution function (BRDF) of the solar diffuser was only measured (incompletely) for Bands 4 and 8 during the prelaunch instrument characterization, and since SeaWiFS does not have a means of measuring the diffuser BRDF on orbit, the OBPG has developed a set of empirical corrections to the solar time series for the effects of the β angle variation, the orbit node drift, and the solar diffuser degradation. The fully calibrated solar data have the long-term radiometric corrections, the Earth–Sun distance corrections, and the solar β angle corrections, and the solar diffuser reflectance degradation corrections applied:

$$L_{\text{Solar}}(\lambda, t) = L_T(\lambda, t)K_{\text{rc}}(\lambda, t)K_{\text{es}}(t)K_{\beta}(\lambda, t)K_{\text{diff}}(\lambda, t), \quad (21)$$

where

K_{rc}	\equiv long-term radiometric correction
K_{es}	\equiv Earth–Sun distance correction
K_{β}	\equiv β angle correction for the position of the Sun in the sky
K_{diff}	\equiv diffuser reflectance degradation correction

The β angle corrections were derived from multiple linear regressions of the β angle time series and the node drift time series against the diffuser time series. The regression equation, which is the inverse of the β angle correction K_{β} is

$$\frac{1}{K_{\beta}(\lambda, t)} = r_0(\lambda) + r_1(\lambda) \cos(\beta(t)) + r_2(\lambda) \sin(\beta(t)) + r_3(\lambda)\Omega(t), \quad (22)$$

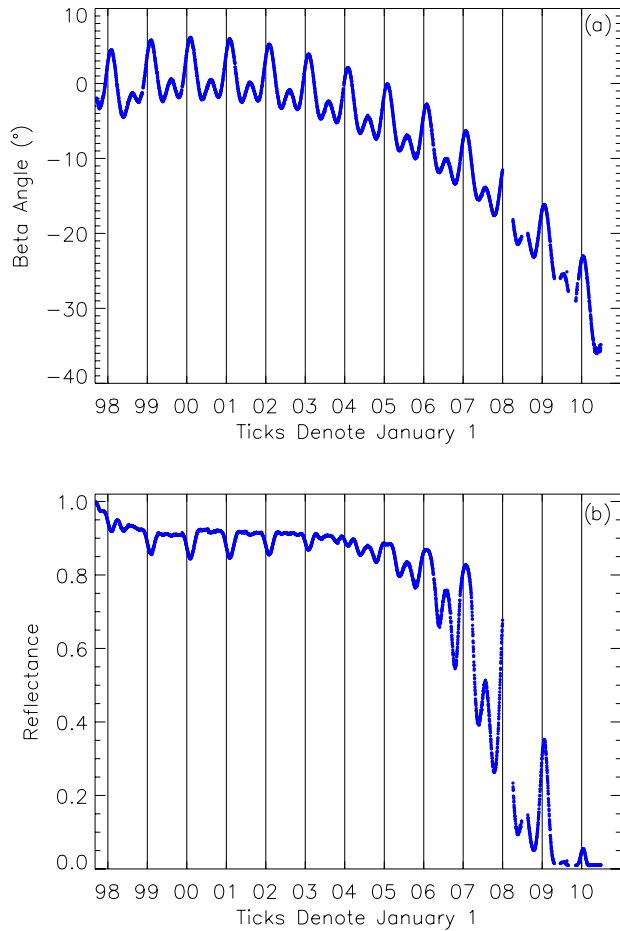


Fig. 14. (Color online) **Solar Calibration Time Series.** (a) The β angle time series shows the temporal trend of the orbit node drift. (b) The Band 1 time series (with the long-term radiometric corrections applied) shows the combined effects of the solar β angle variation, the diffuser reflectance degradation, and the orbit node drift. The node drift causes the image of the Sun to move off of the solar diffuser over time, diminishing the radiance reflected by the diffuser.

where

r_i	\equiv	regression coefficients
β	\equiv	β angle of the Sun on the diffuser
Ω	\equiv	node of the satellite's orbit
λ	\equiv	SeaWiFS band
t	\equiv	time of the solar observation

For the diffuser degradation analysis, the OBPG fit the solar diffuser time series, corrected for the solar β angle, with a decaying exponential function of time for each band. These functions, which are the inverses of the diffuser reflectance correction K_{diff} , have the form

$$\frac{1}{K_{\text{diff}}(\lambda, t)} = a_0(\lambda) - a_1(\lambda)[1 - e^{-a_2(\lambda)(t-t_0)}], \quad (23)$$

where

a_i	\equiv	fit coefficients
λ	\equiv	SeaWiFS band
t	\equiv	the time of the solar observation
t_0	\equiv	the reference time for the time series

The uncertainties in the combined corrections for the β angle and the diffuser reflectances are $\sim 2\%$ [14]. The examination of the mission-long solar diffuser time series shows that short-term changes in the radiometric response of the instrument, on timescales shorter than the lunar calibration time series, were not observed.

A. Signal-to-Noise Ratios

The fully calibrated solar time series provide a unique on-orbit calibration capability to the OBPG: a uniformly illuminated, stable, full-aperture radiance source for SeaWiFS. These data allow the OBPG to calculate the SNR for the instrument on orbit:

$$\text{SNR}(\lambda, t) = \frac{\langle L_{\text{Solar}}(\lambda, t) \rangle}{\sigma(\langle L_{\text{Solar}}(\lambda, t) \rangle)}, \quad (24)$$

where the standard deviations of the mean radiances for the individual diffuser observations serve as the noise estimates. These noise estimates are stable over the mission with changes of less than one count for each band [14]. The SNRs for SeaWiFS are summarized in Table 9, which provides the prelaunch SNRs computed for typical TOA radiances and the SNRs measured on orbit from the solar calibration time series. The prelaunch and on-orbit SNRs are computed for different mean radiances, so the measured SNRs are compared to the output of an empirical sensor noise model. Examination of the computed SNRs shows that there have not been appreciable changes in the SeaWiFS SNRs between the prelaunch and on-orbit determinations.

B. Mirror-Side Reflectance Corrections

The relative mirror-side reflectance for the half-angle mirror is defined as the ratio of the solar diffuser radiance L_{Solar} from a mirror-side i ($i = 1, 2$) to the average radiance from the two mirror sides:

$$\begin{aligned} R_{\text{ms}}(\lambda, i, t) &= \frac{2L_{\text{Solar}}(\lambda, i, t)}{L_{\text{Solar}}(\lambda, 1, t) + L_{\text{Solar}}(\lambda, 2, t)} \\ &= \frac{1}{K_{\text{ms}}(\lambda, i, t)}. \end{aligned} \quad (25)$$

The mirror-side reflectance corrections (K_{ms}) are the inverses of the reflectances or the inverses of fits to the reflectance time series. The prelaunch mirror-side reflectance corrections were a step function for each band and mirror side. As the mirror-side reflectances changed with time, the step-function corrections were updated for Reprocessing R2000.0, replaced by piecewise linear corrections for Reprocessing R2002.0 [20], and replaced by simultaneous exponential functions of time for Reprocessing

Table 9. SeaWiFS Signal-to-Noise Ratios^a

Band	λ (nm)	Prelaunch				On Orbit		
		L_{typ}	SNR Spec	Model SNR	Measured SNR	$\langle L_{\text{Solar}} \rangle$	Model SNR	Measured SNR
1	412	9.10	499	990	940	4.44	736	646
2	443	8.41	674	1091	950	5.19	784	794
3	490	6.56	667	1170	1156	5.45	955	976
4	510	5.64	616	1152	1055	5.33	943	1013
5	555	4.57	581	1069	963	5.18	859	953
6	670	2.46	447	781	798	4.43	572	833
7	765	1.61	455	859	860	3.63	668	857
8	865	1.09	467	726	670	2.99	557	767

^aThe prelaunch SNRs are measured at L_{typ} , while the on-orbit SNRs are measured at $\langle L_{\text{Solar}} \rangle$. The radiance units are $\text{mW cm}^{-2} \mu\text{m}^{-1} \text{sr}^{-1}$. The table also shows the SNR specification for each band.

R2004.0. The time series of mirror-side reflectances for Band 1 are shown in Fig. 15; Bands 2–8 show similar behavior. The prelaunch and current mirror-side reflectance differences are shown in Table 10; the current differences, at the 1–2 count level (0.1–0.3%), show the size of striping that would occur if these corrections were not implemented. The orbit node drift and resulting change in the solar beta angle after early 2006 resulted in a lower signal on the diffuser and a significant noise increase in the reflectance computation after that time, so the OBPG has fit the mirror-side reflectance time series through April of 2006 using two simultaneous exponential functions of time, as shown in green in the plot. These fits have been propagated forward beyond April 2006.

The uncertainty in the mirror-side reflectance corrections contributes to the precision of the TOA radiances. The OBPG has assessed the uncertainty, which is too small to give rise to stripes in the data, at 0.01%, as is summarized in Table 5.

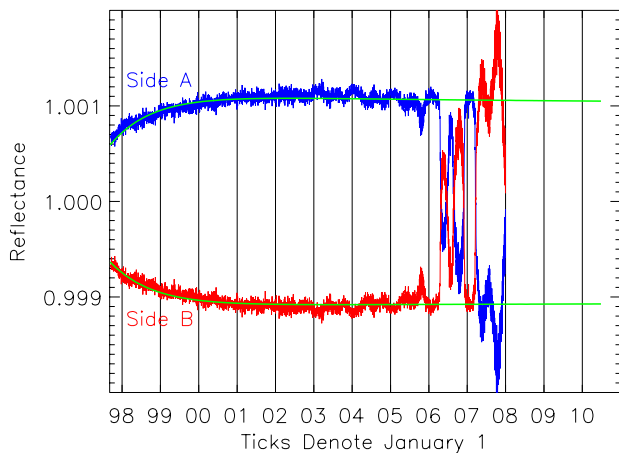


Fig. 15. (Color online) **Band 1 mirror-side reflectances.** The relative reflectances for the two sides of the half-angle mirror. The fits to the data are shown in green (solid fitted line). The low signal due to the orbit node drift and the resulting β angles gives rise significantly higher noise in the time starting in early 2006. Due to the noise in the measurements the data plots stop in early 2008, while the fits are extrapolated to the end of the mission.

C. Detector Calibrations

The SeaWiFS detector calibrations are solar calibrations that have been modified to collect data from each detector individually during the solar measurements, in addition to the data averaged over the four detectors [14,22]. The output averaged over the four detectors in each band is referred to as the ensemble in the following discussion. The OBPG has used the detector calibration time series to look for biases between the individual detectors in each band and the ensemble of detectors for that band and to look for departures in the radiometric response over time of the individual detectors from that of the ensemble. The OBPG analyzed the detector calibration data by computing the ratios of the solar calibration time series for each detector, i ($i = 1, 2, 3, 4$), to the solar calibration time series of the ensemble of detectors, $i = 4:1$:

$$R_{\text{det}}(\lambda, \text{det}_i, t) = \frac{L_{\text{Solar}}(\lambda, \text{det}_i, t)}{L_{\text{Solar}}(\lambda, \text{det}_{4:1}, t)}. \quad (26)$$

The time series for Bands 1, 2, 5, and 6 are shown in Fig. 16. As with the solar calibration data, the orbit node drift makes use of the detector calibration data problematic after 2005. These plots show that for each band, the noise in the cloud detector is higher than the noise in the ocean detectors, which is expected. The plots also show that the changes in the radiometric response of the detectors over time track the behavior of the ensembles. Finally, the plots also show that the cloud detectors typically have the

Table 10. Differences in Relative Mirror-Side Reflectances

Band	λ (nm)	Prelaunch Reflectance	Current Reflectance
		Difference (%)	Difference (%)
1	412	0.118	0.213
2	443	0.135	0.275
3	490	0.032	0.049
4	510	0.105	0.251
5	555	0.025	0.041
6	670	0.086	0.242
7	765	0.014	0.061
8	865	0.169	0.291

largest biases with respect to the ensembles. The detector biases for all eight bands are shown in Table 11. The cloud detector biases for Bands 5 and 6 are the largest for all of the bands, which is why the plots for these two bands are included in Fig. 16. These results show that for all eight bands the cloud detectors do not show any systematic changes in radiometric response that are different from those of the ocean detectors. These results validate the application of long-term radiometric corrections that were derived for the ocean detectors to the cloud detectors alone. In other words, the results validate the stray-light correction of the ocean data, the computation of PAR, and the computation of NDVI and surface reflectances over land.

5. Gain Calibration

Since SeaWiFS observes the Moon at a different set of instrument gains than those used for ocean observations (see Table 4), the radiometric trends derived from lunar observations are applicable to the ocean data as long as the gain ratios are constant or as long as any drifts in the gain ratios are corrected in the ocean data. The SeaWiFS gain calibration uses a constant voltage source (the calibration pulse), injected

into the postdetector electronics, to monitor output of the electronic gains over time [14,21]. The gain calibration data analysis generates time series of gain ratios for each band. The gain ratios (GR1, GR2, GR3, GR4) for a given band are defined relative to Gain 1 as follows:

$$GRX(\lambda, t) = \frac{CP(GX, \lambda, t)}{CP(G1, \lambda, t)}, \quad (27)$$

where X designates the commanded gain (Gain 1, Gain 2, Gain 3, or Gain 4) and CP is the output counts from the band for a commanded gain with the calibration pulse as input. The OBPGE examined the gain ratio time series for possible trends. The mission-averaged on-orbit gain ratios, computed for each band and detector from the calibration pulse time series, agree with the on-orbit gain ratios computed by Eplee *et al.* (2007) [14].

The gain ratios for the commanded lunar gains over the SeaWiFS mission are given in Table 12. The table shows that there is no drift in the gain ratios over the mission for Bands 1–5, a minimal drift for Band 6, a significant drift for Band 7, and a marginally significant drift for Band 8. This analysis is limited by the digitization of the calibration pulse data as it comes out of the instrument electronics, which preferentially affects the longer-wavelength bands. The Band 7, Gain 3 time series is the only gain ratio in all 8 bands that is out of family with the other gain ratios in that band; the Band 7 time series are shown in Fig. 17. The OBPGE has incorporated a correction for the Band 7 Gain 3 drift into the instrument calibration. The Band 8 Gain 3 drift is almost large enough to warrant a correction, as well, but the large quantization error for Band 8 precludes a useful correction from being computed. The form of the Gain 3 drift, which is the inverse of the drift correction K_{g3} that is applied to the Band 7 Earth data, is a quadratic function of time:

$$\frac{1}{K_{g3}(\lambda_7, t)} = A_0(\lambda_7) + A_1(\lambda_7)(t - t_0) + A_2(\lambda_7)(t - t_0)^2, \quad (28)$$

where A_i are the fit coefficients.

The uncertainties in the gain ratio trends over time arise from actual changes in the instrument gains, instability in the calibration pulse output, and quantization error in the red bands. These uncertainties only apply to the Earth data for Band 7, where the gain drift correction is applied. The Band 7 Gain 3 drift correction reduces the uncertainty in the gain ratio trending from 0.201% to 0.148%.

6. Vicarious Calibration

The calibration of Earth data applies the long-term radiometric correction derived from lunar calibration to TOA radiances, with a further correction applied to Band 7 for the Gain 3 drift:

Table 11. Detector Calibrations^a

Band	Detector	Bias (%)	Uncertainty (%)
1 (412 nm)	1 ^b	−0.947	0.175
	2	0.576	0.074
	3	−0.277	0.032
	4	0.239	0.026
2 (443 nm)	1	−0.079	0.084
	2	0.742	0.085
	3	−0.330	0.033
	4 ^b	0.953	0.132
3 (490 nm)	1 ^b	−0.902	0.190
	2	0.014	0.057
	3	−0.337	0.029
	4	0.177	0.021
4 (510 nm)	1	0.066	0.080
	2	0.075	0.059
	3	−0.082	0.041
	4 ^b	2.001	0.165
5 (555 nm)	1 ^b	3.570	0.315
	2	−0.455	0.039
	3	0.609	0.042
	4	−0.350	0.030
6 (670 nm)	1	0.537	0.111
	2	−0.810	0.049
	3	1.453	0.091
	4 ^b	−4.176	0.264
7 (765 nm)	1 ^b	−0.874	0.396
	2	0.144	0.072
	3	−0.973	0.054
	4	1.421	0.101
8 (865 nm)	1	1.099	0.267
	2	0.547	0.099
	3	−1.032	0.162
	4 ^b	−0.492	0.262

^aThe biases of the individual detector time series compared to the ensemble time series for the band.

^bDenotes cloud detectors.

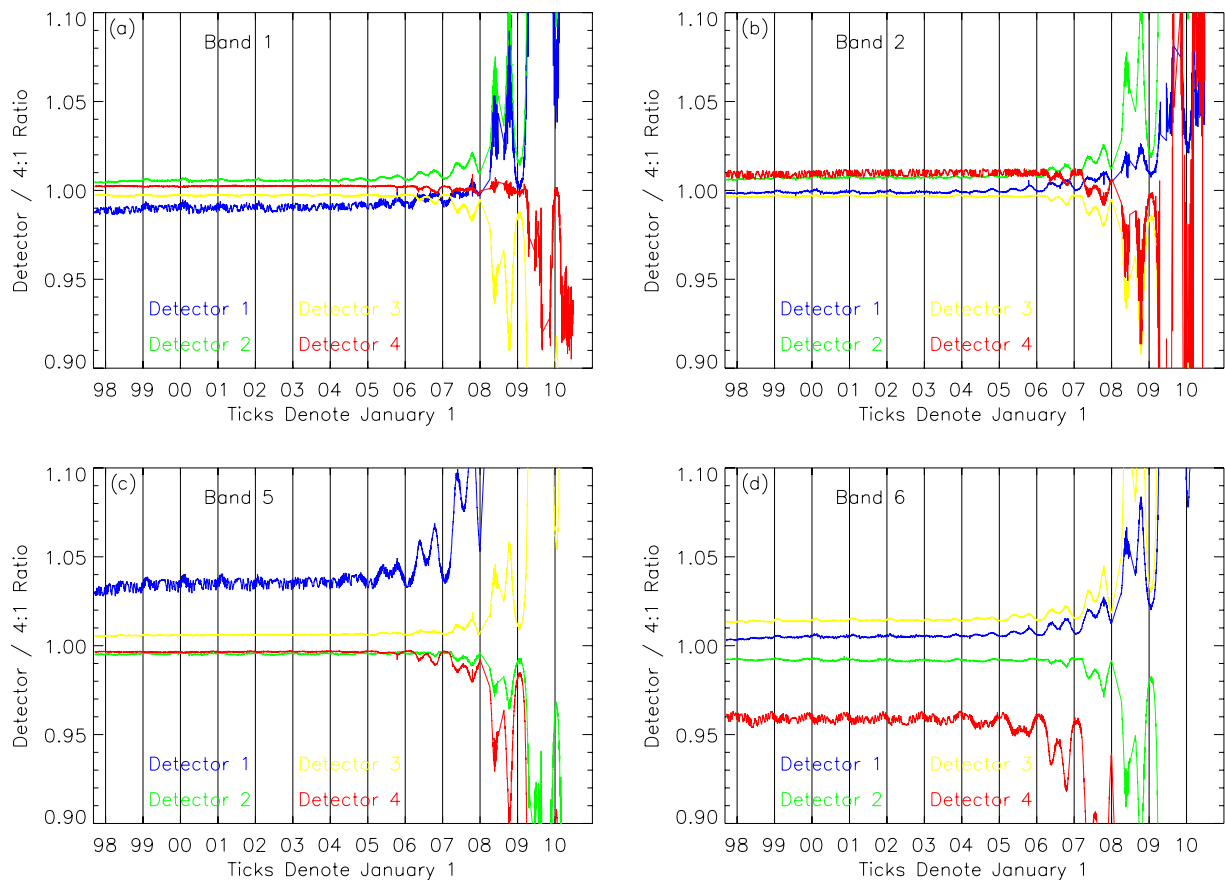


Fig. 16. (Color online) **Detector Calibrations.** (a) and (b) The detector calibration time series for Bands 1 and 2. (c) and (d) The detector calibration time series for Bands 5 and 6. The departure of the cloud detectors from the ensemble for these two bands are the maximum departures observed for any detectors in all eight bands.

$$L_{\text{Earth}}(\lambda_{1-6,8}, t) = L_T(\lambda, t)K_{\text{rc}}(\lambda, t)$$

$$L_{\text{Earth}}(\lambda_7, t) = L_T(\lambda_7, t)K_{\text{rc}}(\lambda_7, t)K_{g3}(\lambda_7, t), \quad (29)$$

where

L_T	\equiv	TOA radiance
K_{rc}	\equiv	long-term radiometric correction
K_{g3}	\equiv	Gain 3 drift correction (for Band 7 Earth data only)

The uncertainties in L_{Earth} arise from the RMS error in the radiances, from the calibration biases,

from the long-term stability of radiometric correction, and for Band 7, from the uncertainty in the Gain 3 drift correction. Various aspects of the vicarious calibration of TOA Earth radiances are discussed in this section of the paper.

A. Derivation of Vicarious Gains

Addressing specific scientific questions about the Earth's climate based on satellite observations of the Earth requires that the TOA radiances of remote sensing instruments be VC to yield accurate results

Table 12. Lunar Gain Ratios^a

Band	λ (nm)	Gain	Gain Ratio	Initial Counts	Final Counts	RMS Error (%)
1	412	4	1.597	614	608	0.0598
2	443	3	1.292	492	478	0.0602
3	490	3	0.9010	329	324	0.0732
4	510	3	0.7975	290	282	0.103
5	555	3	0.6582	239	233	0.110
6	670	3	0.4016	145	143	0.143
7	765	3	0.3393	119	117	0.201
						0.148 ^b
8	865	3	0.2942	109	108	0.174

^aThe gain ratios for lunar calibrations are given for each band. The calibration pulse counts from which the ratios were derived are provided for the start and end of the missions. The long-term stability of the gain ratios are provided.

^bThe Band 7 stability is also provided after the Gain 3 drift correction.

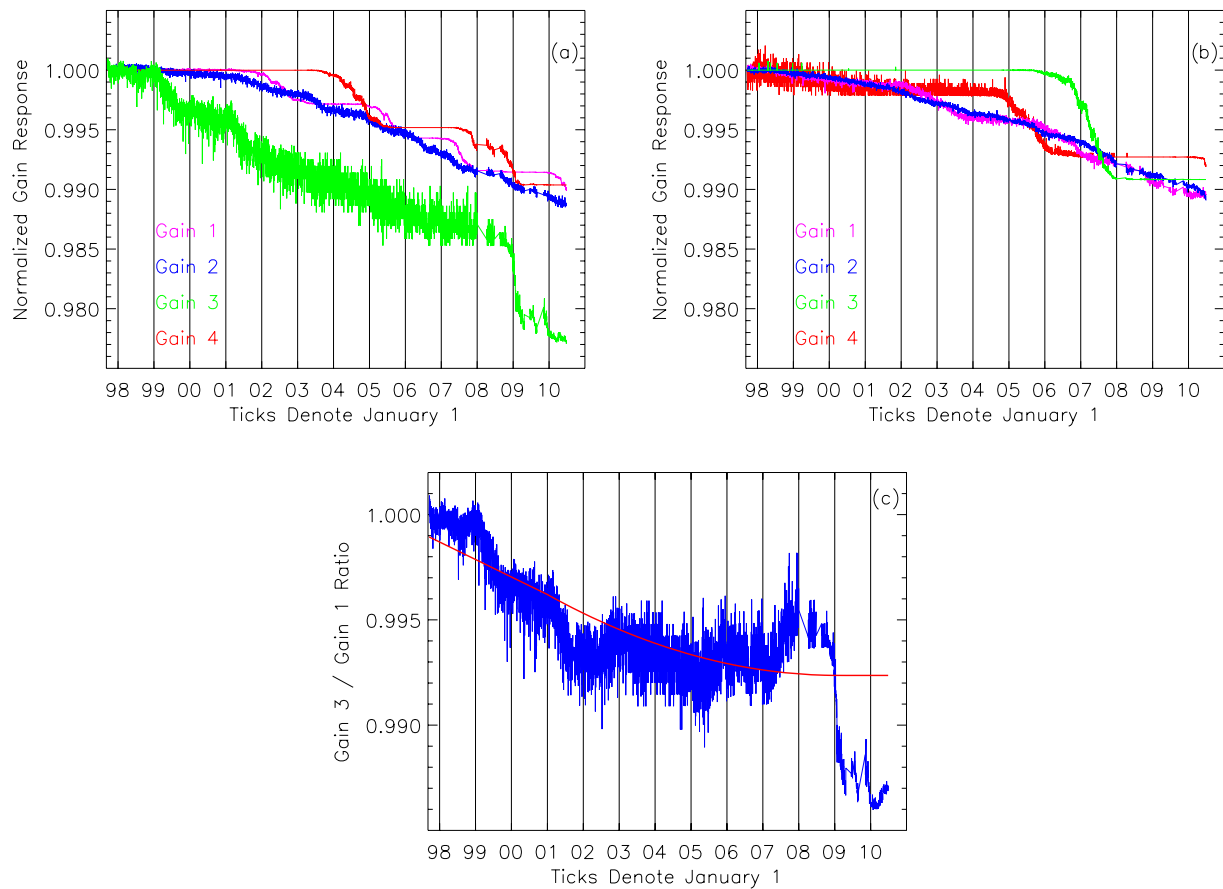


Fig. 17. (Color online) **Bands 7 and 8 gain calibrations.** (a) The Band 7 time series; Gain 3 is the only gain in all eight bands that is out of family with the other gains in that band. (b) The Band 8 time series; Gain 3 is impacted by digitization noise. (c) The Band 7 Gain 3/Gain 1 drift correction for the ocean color data are shown in red.

at the surface of interest. For example, the vicarious calibration of ocean color data adjusts the on-orbit calibration of the instruments to match the system-level calibration of the *in situ* radiometer and atmospheric correction algorithm [5]. The vicarious calibration mitigates uncertainties (e.g., biases) in the calibration of the satellite instrument, the calibration of the *in situ* radiometer, and the atmospheric correction algorithm. By adjusting the calibration of the SeaWiFS TOA radiances (with

the long-term radiometric correction already applied) so that the retrieved SeaWiFS water-leaving radiances match corresponding in-water measurements from MOBY, the vicarious calibration provides a means of cross calibrating SeaWiFS with the MOBY/atmospheric correction algorithm. As a counter example, atmospheric data products may not require any vicarious calibration of the TOA radiances.

For the first Reprocessing (R1998.0), the OBPG implemented a forward vicarious calibration procedure

Table 13. Vicarious Calibration^a

Band	λ (nm)	NIST Gains	SBRS Gains	Calibration Bias (%)	Gain Uncertainty (%)	MOBY Uncertainty (%)
1	412	1.0368 ^b	1.0066 ^b	-0.656	0.07	2.4
2	443	1.0132 ^b	0.9983 ^b	0.170	0.07	2.1
3	490	0.9918 ^b	0.9892 ^b	1.09	0.07	2.4
4	510	0.9982 ^b	0.9924 ^b	0.766	0.07	2.3
5	555	0.9993 ^b	1.0047 ^b	-0.468	0.07	2.4
6	670	0.9729 ^b	0.9799 ^b	2.05	0.06	3.3
7	765	0.9716 ^c	0.9700 ^c	3.09	0.11	
8	865	1.00 ^d	1.00 ^d			

^aThe NIST-based vicarious gains were derived using the NIST-measured counts-to-radiance conversion coefficients, while the SBRS-based vicarious gains were derived using the SBRS-measured counts-to-radiances conversion coefficients.

^bGains derived from MOBY radiances propagated to the TOA.

^cGains derived from aerosol retrievals.

^dNo vicarious calibration. The MOBY uncertainties are for the water-leaving radiances.

for the visible bands (Bands 1–6), which compared water-leaving radiances (L_w) between SeaWiFS and MOBY at the ocean surface to determine the vicarious gains [23]. This procedure required an iterative approach, with the vicarious gains being adjusted between retrievals of L_w for SeaWiFS until the SeaWiFS/MOBY radiances converged. The NIR band vicarious calibration adjusted the Band 7 vicarious gain to retrieve the expected aerosols for open ocean scenes in the vicinity of MOBY. Inefficiencies in the visible band calibration led the OBPG to develop a method of propagating the MOBY L_w to the top of the atmosphere using the parameters retrieved by the atmospheric correction algorithm, thus allowing the vicarious gains to be computed directly from the MOBY and SeaWiFS TOA radiances on a per-match-up basis [5]. To broaden the atmospheric conditions under which the NIR band calibration is valid, the OBPG expanded the size of the open ocean data set from which the Band 7 gain is calibrated. The OBPG implemented these revised vicarious calibration procedures for Reprocessing 2002.0.

The revised SeaWiFS vicarious calibration procedure for ocean color data is:

(1) The calibration of Band 8 (865 nm) is assumed to be correct. The Band 8 gain can be off by ~5% without introducing a significant error into the vicarious calibration [24,25], as will be discussed later in this section of the paper.

(2) Band 7 (765 nm) is calibrated relative to Band 8 so that the atmospheric correction algorithm retrieves the expected aerosol types and optical depths for a set of globally distributed open ocean scenes.

(3) The vicarious gain for the visible bands are computed from ratios of the MOBY L_w , propagated to the top of the atmosphere using the retrieved atmospheric correction parameters, to the SeaWiFS TOA radiances.

Vicarious calibration yields the optimum water-leaving radiances for the sensor/algorithm system-level calibration. The vicarious gains for Bands 1–6 are the mission-long averages of the ratio of the water-leaving radiances measured by MOBY and propagated to the top of the atmosphere to the TOA radiances measured by SeaWiFS [5]:

The VC TOA radiances are

$$\begin{aligned} L_{V\text{Earth}}(\lambda_{1-6}, t) &= L_T(\lambda, t)K_{rc}(\lambda, t)K_{vc}(\lambda) \\ L_{V\text{Earth}}(\lambda_7, t) &= L_T(\lambda_7, t)K_{rc}(\lambda_7, t)K_{g3}(\lambda_7, t)K_{vc}(\lambda_7) \\ L_{V\text{Earth}}(\lambda_8, t) &= L_T(\lambda_8, t)K_{rc}(\lambda_8, t), \end{aligned} \quad (31)$$

where K_{vc} = vicarious gains (for Bands 1–7 Earth data only). The uncertainty in calibrated radiances $L_{V\text{Earth}}$ arises from the RMS error in the radiances, the calibration biases for SeaWiFS, the uncertainty in the Gain 3 drift correction (for Band 7 only), and the uncertainty in the vicarious calibration (for Bands 1–7). The uncertainty in the vicarious calibration itself has two sources: the vicarious gains and the water-leaving radiances measured by MOBY, then propagated to the top of the atmosphere. The uncertainty in the vicarious gains arises from the uncertainty in the atmospheric correction [4,26]. The uncertainties for individual vicarious calibration data points are up to ~1%, but with the collection of 20–40 data points the vicarious gains have converged to values that have uncertainties of 0.1% [5]. The uncertainty in the water-leaving radiances is 2.1–3.3% (depending on the band), which becomes 0.21–0.33% when propagated to the top of the atmosphere [27]. Table 13 shows the vicarious calibration used in the final reprocessing (R2010.0) of the SeaWiFS global ocean color dataset.

B. Calibration of Band 8 (865 nm)

The OBPG has undertaken several analyses of the on-orbit calibration of the 865 nm band. The difficulty in the vicarious calibration of this band is that the only atmospheric correction parameter that the Band 8 calibration impacts directly is the aerosol radiance; the parameter that is actually retrieved by the atmospheric correction algorithm is the aerosol optical depth (AOD) at 865 nm. The initial assessment of the Band 8 calibration came from an analysis of aerosols in the Southern Ocean and set an upper limit on the uncertainty in the Band 8 calibration at 5% high [17]. A vicarious calibration of Band 8 using *in situ* water-leaving radiances from MOBY and aerosol measurements from the AEROSOL ROBOTIC NETwork (AERONET [28,29]) sun photometer on

$$K_{vc}(\lambda, t) = \left\langle \frac{L_w(\lambda, t)t_w(\lambda, t) + L_f(\lambda, t)t_f(\lambda, t) + L_r(\lambda, t)t_r(\lambda, t) + L_a(\lambda, t)t_a(\lambda, t)}{L_{\text{Earth}}(\lambda, t)} \right\rangle, \quad (30)$$

where

L_w	≡	water-leaving radiance measured by MOBY
L_f	≡	sea foam and whitecap radiance
L_r	≡	Rayleigh radiance
L_a	≡	aerosol radiance
t_i	≡	atmospheric transmission for radiance component <i>i</i> .

Lanai showed the Band 8 calibration was 5% high [30]. Subsequent studies of the SeaWiFS global AOD, comparing the SeaWiFS retrievals with *in situ* aerosol measurements from AERONET verified this result [31].

The OBPG performed a set of vicarious calibration sensitivity tests where the vicarious gain of Band 8 was set to 0.95 and 1.05 [23]. In both cases, the vicarious calibration adjusted the vicarious gain of Band 7 to maintain the aerosol retrievals over the open ocean and adjusted the vicarious gains of Bands 1–6 to keep the SeaWiFS water-leaving radiance retrievals in agreement with MOBY. Since the SeaWiFS atmospheric correction algorithm is largely unaffected by uncertainties in the calibration of Band 8 of up to 5% [24,25], the OBPG has never had a justifiable reason to adopt a vicarious gain for Band 8 that departed from unity.

C. Bilinear Gain Knee Calibration

Early during the mission the OBPG discovered that histograms of cloud-top radiances showed discontinuities in the distributions of radiances in the vicinity of the knees of the bilinear response functions (Fig. 4) for all eight bands [32]. These discontinuities resulted from uncertainties in determining the instrument counts at which saturation occurs for the ocean detectors during the prelaunch calibration. The prelaunch calibration of SeaWiFS was performed at four radiance levels, which were either below or above the knee radiances [15]; the saturated counts were computed as part of the instrument calibration. Sunlight reflected from cloud tops provides a continuum of radiances in the vicinity of the knees. The OBPG was able to adjust the counts at which saturation occurs for each detector, yielding the smoothest distribution of radiances across the knees possible for each band. The changes in the saturated counts range over 0.0–1.8 counts, with a mean of 0.6 counts. The typical change in the radiances below the knee for the revised saturated counts is 0.1%, while the typical change in the radiances above the knee is 0.8%. While the adjusted knee counts have little effect on the ocean data, they improve the determination of the radiances of aerosols and clouds in the vicinity of and above the knees in the bilinear response. The revised saturated counts were incorporated into the instrument calibration for Reprocessing 2000.0.

D. Response versus Scan Angle

The RVS for the SeaWiFS half-angle mirror was measured during the prelaunch characterization of the instrument, with an uncertainty of 0.3% [13]. Due to the focal plane design discussed above, there are two RVS functions, one for the leading bands on a focal plane (the odd-numbered bands) and one for the trailing bands on a focal plane (the even-numbered bands). These two RVS functions are plotted in Fig. 18. No significant mirror-side differences have been observed in the measured RVS. The half-angle mirror is protected by the telescope housing to minimize the changes in the RVS on orbit. Figure 19 shows the time series of phase angles and scan angles of the full set of lunar calibrations, including nominal and high phase angle observations, denoting the

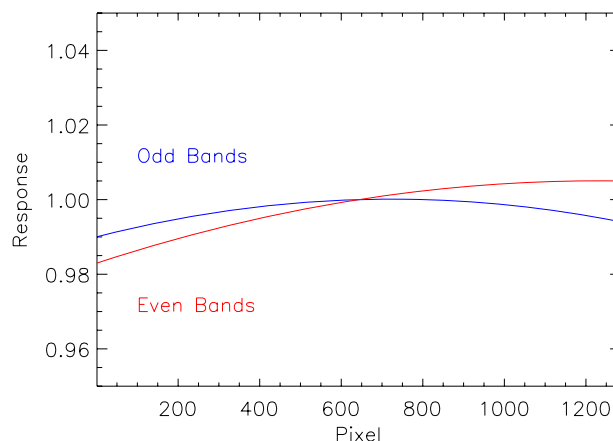


Fig. 18. (Color online) **Response Versus Scan Angle.** SeaWiFS has odd-numbered band and even-numbered band RVS functions. These functions are based on prelaunch characterization measurements made at seven scan angles centered on nadir. The functions are normalized to a value of unity at nadir, so the maximum RVS effect is at either end of scan.

before (blue; lower or left) and after (red; upper or right) full phase observations. Since SeaWiFS is in an orbit with a descending node, negative scan angles for the instrument correspond to positive lunar phase angles.

The OBPG has used a number of vicarious techniques to look for changes in the RVS on orbit:

(1) Lunar residuals for the full lunar time series were examined for RVS effects in the instrumental response. The Band 8 residuals are shown as a function of phase and scan angle in Fig. 19, along with binned versions of the dataset. The calibration bias between Band 8 and the ROLO model is evident in the plots. While the high phase and scan angle observations show more scatter, there is no significant trend in the data as a function of phase or scan angle.

(2) Water-leaving radiances, aggregated as a function of pixel number in the scan, were examined for RVS effects, but separating changes in the RVS from uncertainties in the ocean BRDF or from uncertainties in the atmospheric correction algorithm have proven to be difficult [23].

(3) Cloud-top radiances for deep convective clouds, aggregated as a function of pixel number in the scan, were examined for RVS effects with inconclusive results.

So, the OBPG has concluded that there is not any reliable evidence of change in the RVS on orbit, so the uncertainty in the RVS remains at the prelaunch characterization value of 0.3%, as summarized in Table 5. This RVS analysis for SeaWiFS validates the ROLO model's residual phase dependence at 1% or less, as was reported for the SeaWiFS/MODIS cross calibration using the Moon [16].

E. Counts-to-Radiance Conversion Coefficients

As planning and testing began for SeaWiFS Reprocessing R2009.0, a concern was raised within the

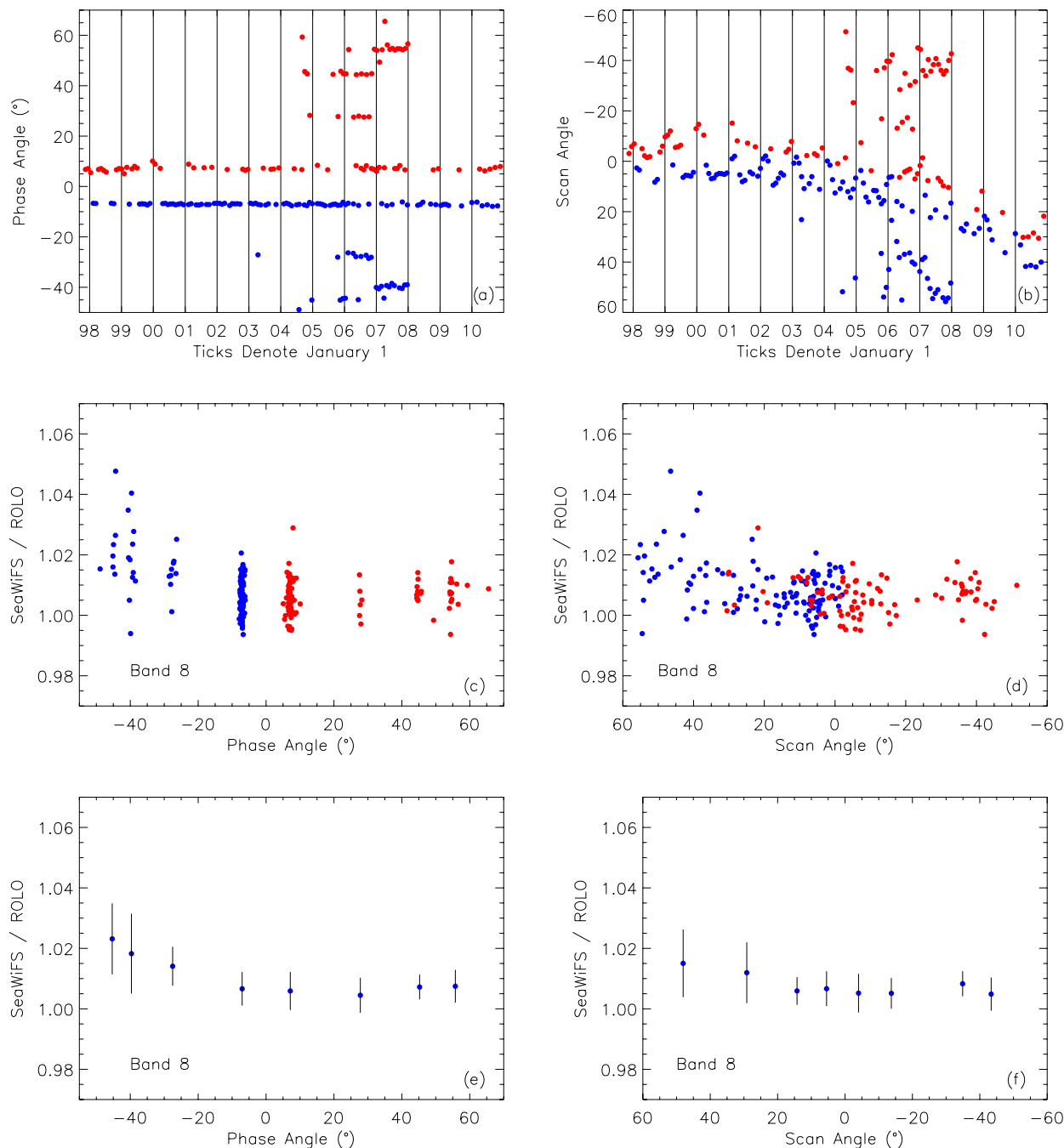


Fig. 19. (Color online) **RVS Evaluation.** Before (blue; lower or left) and after (red; upper or right) full phase. (a) The time series of phase angles of the lunar observations. (b) The corresponding time series of scan angles of the lunar observations. (c) The Band 8 lunar residuals as a function of phase angle. (d) The Band 8 lunar residuals as a function of scan angle. (e) The residuals binned as a function of phase angle. (f) The residuals binned as a function of scan angle. The lunar residuals do not show any significant trends with phase angle or scan angle.

OBPG about the relative size of the vicarious gains for the SeaWiFS visible bands compared with those derived for Aqua MODIS, particularly the large gains for Bands 1 and 2, as shown in Fig. 20. These apparently anomalous vicarious gains brought into question the values of the counts-to-radiance conversion coefficients, since the the combined gain of the vicarious calibration is the product of the prelaunch counts-to-radiance conversion coefficient (K_c) and the vicarious gain G_{vic} :

$$G_{comb}(\lambda) = K_c(\lambda)G_{vic}(\lambda). \quad (32)$$

In one sense, how the combined gain is partitioned between the counts-to-radiance conversion coefficients and the vicarious gains is arbitrary. The normal expectation is that the prelaunch calibration should result in vicarious gains that are close to unity, as is the case with Aqua MODIS. Instead, the SeaWiFS vicarious gains showed an unexpected significant trend with wavelength.

While exploring possible causes for this trend, the OBPG looked at the comparisons between the 1997 prelaunch calibration of SeaWiFS conducted by NIST during the integration of the instrument with the spacecraft [15] and the 1993 prelaunch calibration of SeaWiFS conducted by SBRS during the instrument development [13]. The OBPG has used the NIST prelaunch calibration for SeaWiFS from the launch of the instrument through Reprocessing R2007.0. The comparison of the counts-to-radiance coefficients K_c for Gain 1 derived by the two calibrations, as computed by Johnson *et al.* (1999) [15], is shown in Fig. 20(a). The plot shows a trend with wavelength in the opposite direction of the trend in the vicarious gains, as would be expected if the gain trend is due to a trend in the counts-to-radiance coefficients. To examine the change in the TOA radiances for SeaWiFS that would result from changing the prelaunch calibration, the OBPG derived a set of mission-long lunar calibration residuals using both sets of counts-to-radiance conversion coefficients, as shown in Fig. 20(b) [33]. The lunar residuals based on the NIST-derived coefficients show a trend with wavelength that does not appear in the residuals

based on the SBRS-derived coefficients. These results are consistent with the trends in the vicarious gains and with the prelaunch calibration comparisons. Figure 20(c) shows that the correlation between the vicarious gains and the lunar ratios for the NIST prelaunch calibration is much higher than the correlation for the SBRS prelaunch calibration, indicative of the trend with wavelength in the NIST calibration. The likely cause of the discrepancies between the NIST prelaunch calibration and the SBRS prelaunch calibration was a drift over time in the calibration of the SeaWiFS Transfer Radiometer (SXR) [34]. The SXR provided the radiance measurements used in generating the counts-to-radiances conversion coefficients for the NIST calibration of SeaWiFS.

The trends in the vicarious calibration coefficients with wavelength and the corresponding trends in the lunar residuals have led the OBPG to adopt the SBRS-derived counts-to-radiance conversion coefficients for the instrument calibration used for Reprocessing R2009.0. The resulting vicarious calibration coefficients are shown in Fig. 20 and in Table 13. As expected, the vicarious gains for Bands 1 and 2 are significantly closer to unity for the SBRS prelaunch

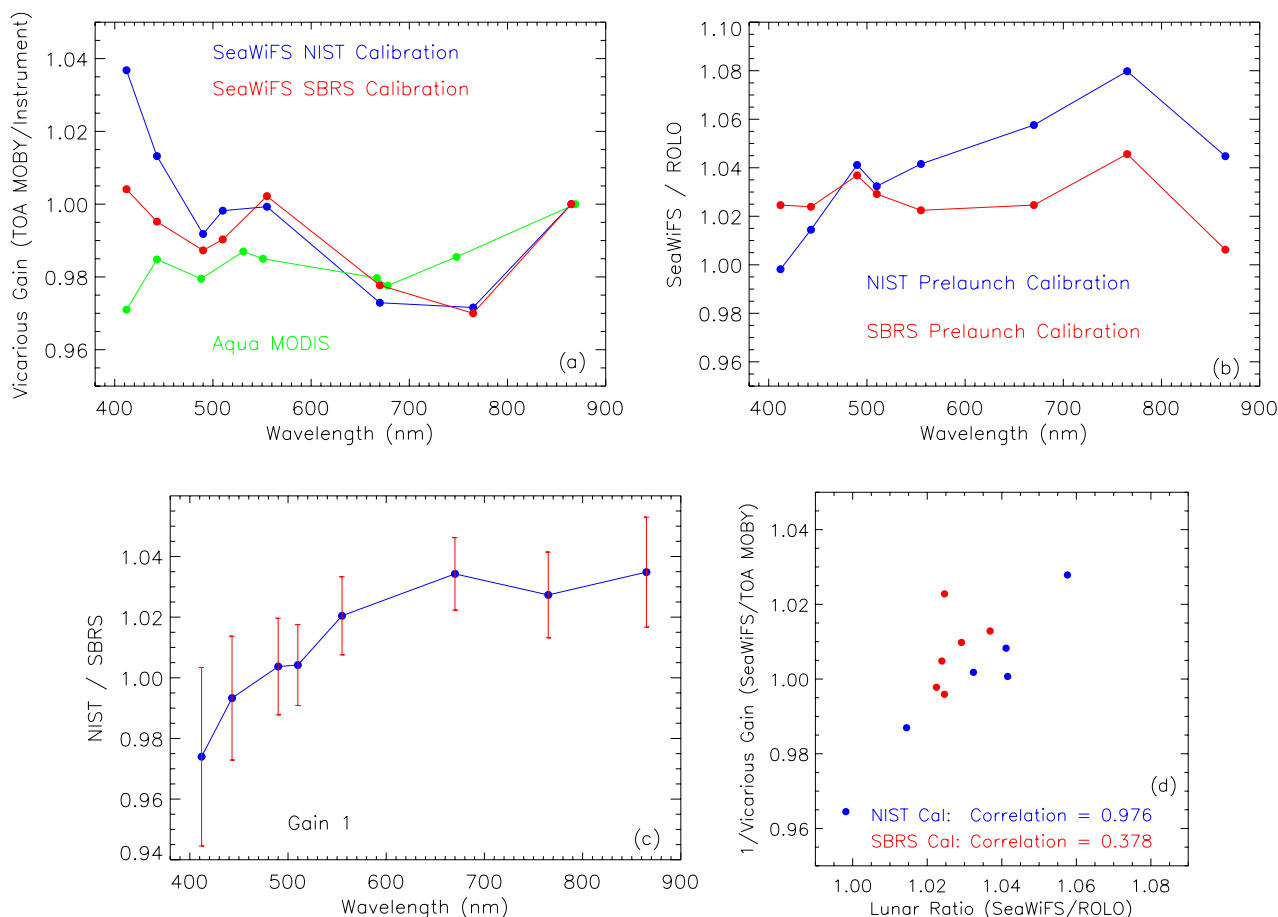


Fig. 20. (Color online) **NIST/SBRS calibration comparisons.** (a) The Aqua MODIS, SeaWiFS NIST-based, and SeaWiFS SBRS-based vicarious gains. (b) The lunar ratios for the NIST and SBRS calibrations. (c) The ratio of the NIST calibration to the SBRS calibration, with errors. (d) The correlation between the vicarious gains and lunar ratios for the NIST and SBRS calibrations. The NIST calibration shows a correlation as a function of wavelength, while the SBRS calibration does not.

calibration than was the case with the NIST pre-launch calibration. This change in counts-to-radiance conversions coefficients does not impact the long-term radiometric corrections for SeaWiFS, which are based on the relative changes in the radiometric response of the instrument, nor does it impact the combined effect of the counts-to-radiance conversion coefficients and the vicarious gains on the SeaWiFS ocean retrievals.

7. Uncertainty in the TOA Radiances

Having reviewed the sources of uncertainty in the SeaWiFS on-orbit calibration and the prelaunch calibration uncertainties (Table 5), this paper will now merge the various uncertainty estimates to present the overall uncertainty in the calibrated TOA radiances. Again, the uncertainty will be addressed in the terms of accuracy or calibration biases, stability or repeatability of the measurements over time, and precision or scatter in the measurements.

A. Accuracy of the TOA Radiances

The mission-averaged mean lunar residuals from the ROLO model and the magnitude of the vicarious calibration gains provide the best on-orbit estimates of the biases in the SeaWiFS TOA radiances that are internal to the SeaWiFS calibration. The measurement accuracy is defined as

$$\text{Accuracy} = \left\langle \frac{\text{SeaWiFS}}{\text{Reference}} - 1 \right\rangle, \quad (33)$$

so the accuracy of the vicarious calibration is derived from the inverses of the vicarious gains, as shown by Eq. (30). Figure 11(b) shows the mean ROLO residuals for the lunar observations and the inverses of the vicarious gains computed relative to MOBY. The trends in the biases with wavelength are comparable, though the biases are smaller for the vicarious calibration. The biases in the SeaWiFS TOA radiances are shown in Table 14. The average bias in the lunar calibration is $2.62 \pm 1.16\%$. The average bias in the vicarious calibration for Bands 1–7 is $1.19 \pm 1.03\%$. In summary, the accuracy of the SeaWiFS TOA radiances is 2–3% relative to the ROLO model or 1–2% relative to MOBY. For comparison purposes, the uncertainty in the NIST prelaunch calibration of SeaWiFS is 4% [15], and the cross calibration of SeaWiFS relative to Terra MODIS and Aqua MODIS on orbit is 3–8% [16]. The measured accuracy of the SeaWiFS TOA radiances is within the uncertainties of the prelaunch calibration. The key question that remains unanswered in the accuracy or bias determination is one of bias compared to which external reference? The specific scientific question being addressed determines the external reference for the calibration bias.

B. Long-Term Stability of the TOA Radiances

The long-term stability of the TOA radiances is a validation of the effectiveness of the radiometric

Table 14. On-Orbit Measurement Accuracy^a

Band	λ (nm)	SeaWiFS/ROLO Bias (%)	SeaWiFS/MOBY Bias (%)
1	412	2.35 ± 0.12	-0.656 ± 0.07
2	443	2.25 ± 0.078	0.170 ± 0.07
3	490	3.68 ± 0.033	1.09 ± 0.07
4	510	2.90 ± 0.046	0.766 ± 0.07
5	555	2.22 ± 0.058	-0.468 ± 0.07
6	670	2.43 ± 0.096	2.05 ± 0.06
7	765	4.52 ± 0.12	3.09 ± 0.11
8	865	0.60 ± 0.13	

^aThe third column shows the SeaWiFS bias relative to the ROLO model. The fourth column shows the SeaWiFS bias relative to MOBY. The uncertainty in the NIST prelaunch calibration is 4% [15].

correction K_{rc} and is a measure of the degree to which a single-point vicarious calibration is applicable to the Earth data. The uncertainty in the long-term stability arises from any residual time dependence in the TOA radiances. Accordingly, the limits on the residual time drift in the fully calibrated lunar time series provide the best on-orbit estimate of the long-term stability of the SeaWiFS TOA radiances. The standard deviation of the mean (or RMS error) of the mission-averaged lunar time series for each band defines the upper limit on the residual time drift in that band, so the actual calibration stability could be better than the RMS error.

As has been discussed previously in this paper, certain systematic errors in the lunar observations that are not present in the Earth observations, namely the uncertainties from the oversampling corrections and the viewing geometry corrections, give rise to errors in the lunar data that are correlated from band to band, and as such, can be mitigated through the coherent noise correction. The coherent noise correction is necessary to derive the true instrumental scatter in the lunar radiances. Figure 10(a) shows the fully calibrated lunar time series with the coherent noise correction applied. The long-term stability (or RMS error) in the lunar time series, before and after coherent noise correction has been applied, is shown in Table 15. Similar RMS errors in each band ($\sim 0.570\%$) before the noise correction are indicative of the coherence in the noise between bands. The reduction in the coherent noise is optimized toward the bands used in computing the noise corrector, so a long-term stability of 0.13% for the SeaWiFS calibration is a reasonable assessment of the instrument performance across all bands. Because of the Band 7 Gain 3 drift, the long-term stability for Band 7 combines the RMS error from the lunar time series (0.116%) with the RMS error in the gain drift correction (0.148%) to yield a long-term stability for the TOA radiances of 0.19%. It should be noted that the coherent noise correction improves the OBPG's ability to compute the long-term stability of the TOA radiances by a factor of ~ 5 .

The long-term stability of the VC TOA radiances that are input to the ocean color retrieval algorithms

Table 15. Long-Term Stability of the Radiometric Calibration^a

Band	λ (nm)	RMS Error (%)	RMS Error (%)
		Before K_{cn}	After K_{cn}
1	412	0.592	0.124
2	443	0.562	0.0778
3 ^b	490	0.579	0.0334
4 ^b	510	0.570	0.0456
5 ^b	555	0.562	0.0578
6	670	0.564	0.0958
7	765	0.554	0.116
			0.188 ^c
8	865	0.567	0.129

^aThe RMS errors before and after the coherent noise correction.

^bBands used to compute the coherent noise correction.

^cError including the Gain 3 drift uncertainty.

combines the uncertainty in the lunar-derived radiometric correction, the uncertainty in the vicarious gains (or atmospheric correction), and the uncertainty in the water-leaving radiances measured by MOBY (then propagated to the top of the atmosphere). As shown in Table 16, the long-term stability becomes the root-sum-square of these three uncertainties: the radiometric correction (from Table 15), the vicarious gains (from Table 13), and the water-leaving radiances from MOBY (Table 13) [27]. For Band 7 the long-term stability combines the uncertainty of the radiometric correction, the uncertainty in the Gain 3 drift correction, and the uncertainty in the vicarious gain of Band 7. There is no vicarious calibration for Band 8. Accordingly, the long-term stability of the VC TOA radiances for Bands 1–6 is 0.30% and for Band 7 is 0.22%. It should be noted that the dominant term in the long-term stability in the VC TOA radiances arises from the vicarious calibration data source, MOBY.

C. Precision of the TOA Radiances

The scatter in the on-orbit measurements made by SeaWiFS gives the precision of the TOA radiances. The SNRs determined from the solar diffuser measurements, and the scatter in the lunar residuals (with the coherent noise correction applied) and are two estimates of the precision of the SeaWiFS on-orbit measurements. The solar diffuser SNR analysis

Table 16. Long-Term Stability of the Vicarious Calibration^a

Band	λ (nm)	Radiometric Correction	Vicarious Gain	MOBY TOA Radiances	Combined RMS Error
		K_{rc}	K_{vc}		
1	412	0.124	0.07	0.24	0.28
2	443	0.0778	0.07	0.21	0.24
3	490	0.0334	0.07	0.24	0.26
4	510	0.0456	0.07	0.23	0.25
5	555	0.0578	0.07	0.24	0.26
6	670	0.0958	0.06	0.33	0.35
7	765	0.188 ^b	0.11		0.22 ^b
8	865	0.129			

^aThe table entries are RMS errors (%).

^bError including the Gain 3 drift uncertainty.

Table 17. On-Orbit Measurement Precision^a

Band	λ (nm)	Solar-derived Precision (%)	Lunar-derived Precision (%)	Vicarious Gain Precision (%)
1	412	0.155	0.124	0.07
2	443	0.126	0.0778	0.07
3	490	0.102	0.0334	0.07
4	510	0.0987	0.0456	0.07
5	555	0.105	0.0578	0.07
6	670	0.120	0.0958	0.06
7	765	0.117	0.116	0.11
8	865	0.130	0.129	

^aThe solar-derived and lunar-derived precision are instrumental properties. The vicarious gain precision is a property of the atmospheric correction algorithm.

results are shown in Table 9, while the RMS error in the lunar residuals are shown in Table 15. The corresponding precision estimates for the SeaWiFS TOA radiances are shown in Table 17. The diffuser-derived estimates of precision are the inverses of the SNR. A reasonable assessment of the precision of the solar diffuser measurements is 0.16%. As has been discussed previously, a reasonable assessment of the precision of the lunar observations is 0.13%. The larger value for the solar precision arises in part because the solar-derived SNR measurements were made for radiances below L_{typ} . The solar-derived precision measurements are consistent with the lunar-derived precision measurements with the coherent noise correction applied, verifying that the coherent noise correction does mitigate systematic errors in the lunar time series arising from the oversampling and geometry corrections. Accordingly, a precision of 0.13% for the SeaWiFS calibration is a reasonable assessment of the instrument performance across bands.

The scatter in the vicarious gains gives the precision of the vicarious calibration, as is shown in Table 17. As was noted in the previous section, the uncertainty in the vicarious gains arises from the uncertainty in the atmospheric correction. The precision of the vicarious calibration directly determines the number of data points in the calibration required for the vicarious gains to converge [5]. For the vicarious calibration of SeaWiFS against MOBY, 30 (Band 2), 40 (Band 5), and 20 (Band 7) data points were required for the gains to converge. Consequently, the OBP required 2–3 years of on-orbit data collection to vicariously calibrate SeaWiFS.

D. Combined Uncertainty Analysis

The goal of this paper has been to examine the on-orbit calibration of SeaWiFS and to assess the resulting uncertainties in the SeaWiFS TOA radiances, the radiances that are the basis of the ocean color data products. The calibration history and associated reprocessing history (summarized in Table 2) show that many calibration artifacts only become apparent, and correctable, over time. The uncertainty assessment has been made in terms of accuracy (biases in the measurements), stability (repeatability of the measurements over time), and precision (scatter in

Table 18. SeaWiFS TOA Uncertainty Assessment^a

Uncertainty		B1	B2	B3	B4	B5	B6	B7	B8	Overall
Accuracy (%)	ROLO	2.35	2.25	3.68	2.90	2.22	2.43	4.52	0.60	2–3
	MOBY	–0.656	0.170	1.09	0.766	–0.468	2.05	3.09		1–2
Stability (%)	TOA	0.124	0.0778	0.0334	0.0456	0.0578	0.0958	0.188 ^b	0.129	0.13
	VC TOA	0.28	0.24	0.26	0.25	0.26	0.35	0.22 ^b		0.30
Precision (%)	Solar	0.155	0.126	0.102	0.0987	0.105	0.120	0.117	0.130	0.16
	Lunar	0.124	0.0778	0.0334	0.0456	0.0578	0.0958	0.116	0.129	0.13
	Vicarious	0.070	0.070	0.070	0.070	0.070	0.060	0.11		0.10

^aThe accuracy is relative to the ROLO model or to MOBY. The stability is given for TOA radiances and vicariously calibrated (VC) TOA radiances. The precision estimates have the indicated sources. Band 8 does not have a vicarious calibration.

^bIncluding the Band 7 Gain 3 drift correction.

the measurements), as presented in Table 18. The absolute uncertainty is computed relative to the ROLO model for the lunar calibration or relative to MOBY for the vicarious calibration. The long-term stability is provided for the TOA radiances and for the VC TOA radiances. The precision estimates are computed from solar calibrations, lunar calibrations, and the vicarious calibration. The uncertainties in the TOA radiances can be summarized as follows: the accuracy of the TOA radiances relative to the ROLO model of the Moon are 2–3%; the accuracy of the VC TOA radiances relative to MOBY are 1–2%. The long-term stability of the TOA radiances, primarily due to the success of the radiometric correction, is 0.13%. The long-term stability of the VC TOA radiances, which are inputs for the ocean color data retrievals, is 0.30%. The Band 7 Gain 3 drift correction yields TOA radiances for Band 7 with a long-term stability of 0.19% and yields VC TOA radiances for Band 7 with a stability of 0.22%. The precision of the SeaWiFS measurements is 0.13% as computed from the lunar calibrations, 0.16% as computed from the solar calibrations, and is 0.10% as computed from the vicarious calibration. This uncertainty assessment has been developed as the performance of the instrument has changed over time and as our understanding of the instrument performance has evolved, as summarized in Table 2.

8. Summary of the Orbit Node Drift

Since the Orbview 2 satellite did not have an orbit maintenance capability, the spacecraft altitude decayed from an initial value of 705 km in September 1997 to 690 km by of June 2010. Consequently, the node of the orbit node drifted from the start of the mission and the node crossing time has increased from 12:00 noon (September 1997), to 1:00 pm (June 2007), to 2:20 pm (June 2010) (Fig. 2). As the orbit node drifted: (1) the scan angle at which SeaWiFS observed the Moon for a given phase angle increased (Fig. 19); (2) the position of the image of the Sun on the solar diffuser, the β angle, decreased significantly (Fig. 14); and (3) the mean focal plane temperatures for the instrument decreased (Fig. 12). The increase in lunar scan angle caused the track angle of the lunar observations to become significant, thus increasing the uncertainty in the sizes of the lunar images

and the resulting uncertainty in the oversampling corrections (Fig. 8). The solar β angle drift made the solar calibrations (Fig. 14), the mirror-side corrections (Fig. 15), and detector calibrations (Fig. 16) ineffective from 2006 onwards. The lunar scan angle and solar β angle drifts had minimal impacts on the instrument calibration quality. The updated focal plane temperature corrections mitigated the effect of the focal plane temperature trend. The orbit node drift did cause a significant increase in the amount of sun glint observed in the vicinity of the subsolar point for the ocean color data.

To rectify the effects of the orbit node drift on the SeaWiFS data, particularly the increase in sun glint, a series of orbit raising maneuvers were executed by the spacecraft between late June and early July of 2010, increasing the altitude to 782 km and reversing the direction of the node drift (Fig. 2). The orbit raising should have not had any impact on the instrument radiometric calibration. SeaWiFS observed five lunar calibrations after the orbit raising maneuver from July through November of 2010. The lunar time series in Fig. 10 show that these calibrations continue the radiometric trends of the calibrations preceding the orbit raising, as expected. The end of the mission occurred before the impact of the reversed orbit node drift on the solar calibrations or on the sun glint contamination of the ocean color data could be assessed. The SeaWiFS experience with the effects of orbit node drift argue for a spacecraft orbit maintenance capability to maximize the quality of Earth data collected by satellite instruments.

9. Conclusions

This paper documents the 13-year on-orbit calibration history of SeaWiFS. Over the mission, the on-orbit performance of the instrument has evolved while the OBPG's understanding of the instrument calibration has steadily increased. During this time the OBPG has continued to improve the capabilities of the atmospheric correction, ocean color retrieval, and vicarious calibration algorithms. The SeaWiFS calibration and uncertainty assessments show the necessity of a mission-long calibration/validation program for climate quality data to be produced from remote sensing satellite instruments.

SeaWiFS was the first remote sensing satellite instrument to make full use of the Moon as a monitor for on-orbit radiometric performance. The resulting calibration history demonstrates the efficacy of the Moon as an exoatmospheric calibration reference. The dependence of the SeaWiFS lunar calibration quality on the ROLO photometric model of the Moon shows the importance to the U.S. climate research program of continued institutional support for the maintenance and further development of the ROLO photometric model (or similar capability).

From the standpoint of climate research, the most important uncertainty in the TOA radiances measured by a satellite instrument on orbit is the long-term stability of the calibration. For an instrument whose radiometric response changes over time, the stability shows how well the calibration team understands the evolving instrument performance on orbit and how well the long-term radiometric correction accounts for that changing performance. The OBPG has been able to maintain the long-term stability the SeaWiFS calibration at the level of $\sim 0.1\%$ from the initial estimate of the stability 6 years into the mission [7] onwards through the end of the mission at 13 years [16]. The radiometric stability of the TOA radiances at the 0.1% level yields retrievals of water-leaving radiances that are stable at the 1% level, allowing the generation of CDRs from the ocean color dataset.

The SeaWiFS mission has provided the first decadal scale CDR of ocean color data, particularly ocean chlorophyll and phytoplankton biomass [35]. The availability of this long-term, stable, global ocean color dataset has allowed climate researchers to study the global ocean ecosystem and carbon cycle dynamics over time scales where climate change signals become discernable [36–39]. At the same time, the global ocean color dataset has allowed resource managers to improve the sustainability of economically important marine fisheries [40] and to improve the monitoring of harmful algal blooms in coastal waters [41]. Given the relatively short duration of satellite missions relative to the time scales of climate change, the production of CDRs requires a consistent time series of ocean color data across multiple missions [42]. This is an important lesson from SeaWiFS for NASA and NOAA as the production of ocean color data products transitions from research instruments and programs (e.g., SeaWiFS and MODIS) to operational instruments and programs (e.g., VIIRS) [43–45].

The authors wish to thank Tom Stone of the U.S. Geological Survey for discussions about applying the ROLO model to the SeaWiFS lunar datasets. The SeaWiFS calibration uncertainty analysis presented in this paper was originally published in Eplee *et al.* (2011) [46].

References

1. B. A. Franz, S. W. Bailey, G. Meister, and P. J. Werdell, "Quality and consistency of the NASA ocean color data record," *Proc. Ocean Optics XXI*, Glasgow, Scotland, 8–12 October (2012).
2. National Research Council, Climate Data Records from Environmental Satellites: Interim Report (The National Academies, 2004).
3. C. R. McClain, W. E. Esaias, W. Barnes, B. Guenther, D. Endres, S. B. Hooker, G. Mitchell, and R. Barnes, SeaWiFS Calibration and Validation Plan, S. B. Hooker and E. R. Firestone, eds., **3** NASA Tech. Memo. 104566, (NASA Goddard Space Flight Center, 1992).
4. H. R. Gordon, "Atmospheric correction of ocean color imagery in the Earth observing system era," *J. Geophys. Res.* **102**, 17081–17106 (1997).
5. B. A. Franz, S. W. Bailey, P. J. Werdell, and C. R. McClain, "Sensor-independent approach to the vicarious calibration of satellite ocean color radiometry," *Appl. Opt.* **46**, 5068–5082 (2007).
6. H. H. Kieffer, "Photometric stability of the lunar surface," *Icarus* **130**, 323–327 (1997).
7. R. E. Eplee, Jr., R. A. Barnes, F. S. Patt, G. Meister, and C. R. McClain, "SeaWiFS lunar calibration methodology after six years on orbit," *Proc. SPIE* **5542**, 1–13 (2004).
8. H. H. Kieffer and T. C. Stone, "The spectral irradiance of the Moon," *Astron. J.* **129**, 2887–2901 (2005).
9. T. C. Stone and H. H. Kieffer, "Use of the Moon to support on-orbit sensor calibration for climate change measurements," *Proc. SPIE* **6296**, 62960Y (2006).
10. T. C. Stone, "Radiometric calibration stability and inter-calibration of solar-band instruments in orbit using the Moon," *Proc. SPIE* **7081**, 70810X (2008).
11. D. K. Clark, H. R. Gordon, K. J. Voss, Y. Ge, W. Broenkow, and C. Trees, "Validation of atmospheric correction over the oceans," *J. Geophys. Res.* **99**, 7293–7307 (1997).
12. D. K. Clark, M. E. Feinholz, M. A. Yarbrough, B. C. Johnson, S. W. Brown, Y. S. Kim, and R. A. Barnes, "Overview of the radiometric calibration of MOBY," *Proc. SPIE* **4483**, 64–76 (2002).
13. R. A. Barnes, A. W. Holmes, W. L. Barnes, W. E. Esaias, C. R. McClain, and T. Svitek, SeaWiFS Prelaunch Radiometric Calibration and Spectral Characterization, S. B. Hooker, E. R. Firestone, and J. G. Acker, eds. **23**, NASA Tech. Memo. 104566 (NASA Goddard Space Flight Center, 1994).
14. R. E. Eplee, Jr., F. S. Patt, B. A. Franz, S. W. Bailey, G. Meister, and C. R. McClain, "SeaWiFS on-orbit gain and detector calibrations: effect on ocean products," *Appl. Opt.* **46**, 6733–6750 (2007).
15. B. C. Johnson, E. E. Early, R. E. Eplee, Jr., R. A. Barnes, and R. T. Caffrey, The 1997 Prelaunch Radiometric Calibration of SeaWiFS, S. B. Hooker and E. R. Firestone, eds. **4**, NASA Tech. Memo. 206892 (NASA Goddard Space Flight Center, 1999).
16. R. E. Eplee, Jr., J.-Q. Sun, G. Meister, F. S. Patt, X. Xiong, and C. R. McClain, "Cross calibration of SeaWiFS and MODIS using on-orbit observations of the Moon," *Appl. Opt.* **50**, 120–133 (2011).
17. R. A. Barnes, R. E. Eplee, Jr., G. M. Schmidt, F. S. Patt, and C. R. McClain, "Calibration of SeaWiFS. I. Direct techniques," *Appl. Opt.* **40**, 6682–6700 (2001).
18. A. H. Johnston, "Radiation damage of electronic and optoelectronic devices in space," presented at the 4th International Workshop on Radiation Effects on Semiconductor Devices for Space Application, Tsukuba, Japan (11–13, October 2000).
19. R. E. Eplee, Jr., G. Meister, F. S. Patt, and C. R. McClain, "The on-orbit calibration of SeaWiFS: functional fits to the lunar time series," *Proc. SPIE* **7081**, 708112 (2008).
20. R. E. Eplee, Jr., R. A. Barnes, S. W. Bailey, and P. J. Werdell, "Changes to the on-orbit calibration of SeaWiFS," in *Algorithm Updates for the Fourth SeaWiFS Data Reprocessing*, S. B. Hooker and E. R. Firestone, eds. **22**, NASA Tech. Memo. 206892 (NASA Goddard Space Flight Center, 2003), pp. 12–19.
21. R. E. Eplee, Jr., F. S. Patt, G. Meister, B. A. Franz, S. W. Bailey, and C. R. McClain, "The on-orbit calibration of SeaWiFS: revised temperature and gain corrections," *Proc. SPIE* **6677**, 66770E (2007).

22. R. E. Eplee, Jr., R. A. Barnes, and C. R. McClain, "SeaWiFS detector and gain calibrations: Four year of on-orbit stability," *Proc. SPIE* **4814**, 282–288 (2002).
23. R. E. Eplee, Jr., W. D. Robinson, S. W. Bailey, D. K. Clark, P. J. Werdell, M. Wang, R. A. Barnes, and C. R. McClain, "Calibration of SeaWiFS. II. Vicarious techniques," *Appl. Opt.* **40**, 6701–6718 (2001).
24. H. R. Gordon, "In-orbit calibration strategy for ocean color sensors," *Remote Sens. Environ.* **63**, 265–278 (1998).
25. M. Wang and H. R. Gordon, "Calibration of ocean color scanners: how much error is acceptable in the near infrared?," *Remote Sens. Environ.* **82**, 497–504 (2002).
26. Z. Ahmad, B. A. Franz, C. R. McClain, E. J. Kwiatkowska, J. Werdell, E. P. Shettle, and B. N. Holben, "New aerosol models for the retrieval of aerosol optical thickness and normalized water-leaving radiances from the SeaWiFS and MODIS sensors over coastal regions and open oceans," *Appl. Opt.* **49**, 5545–5560 (2010).
27. S. W. Brown, S. J. Flora, M. F. Feinholz, M. A. Yarbrough, T. Houlihan, D. Peters, Y. S. Kim, J. L. Mueller, B. C. Johnson, and D. K. Clark, "The Marine Optical BuoY (MOBY) radiometric calibration and uncertainty budget for ocean color satellite sensor vicarious calibration," *Proc. SPIE* **6744**, 67441M (2007).
28. B. N. Holben, T. F. Eck, I. Slutsker, D. Tanre, J. P. Buis, A. Setzer, E. Vermote, J. A. Reagan, Y. J. Kaufman, T. Nakajima, F. Lavenue, I. Jankowiak, and A. Smirnov, "AERONET—A federated instrument network and data archive for aerosol characterization," *Remote Sens. Environ.* **66**, 1–16 (1998).
29. B. N. Holben, D. Tanre, A. Smirnov, T. F. Eck, I. Slutsker, N. Abuhassan, W. W. Newcomb, J. S. Schafer, B. Chatenet, F. Lavenue, Y. J. Kaufman, J. Vande Castle, A. Setzer, B. Markham, D. Clark, R. Frouin, R. Halthore, A. Karneli, N. T. O'Neill, C. Pietras, R. T. Pinker, K. Voss, and G. Zibordi, "An emerging ground-based aerosol climatology: aerosol optical depth from AERONET," *J. Geophys. Res.* **106**, 12067–12097 (2001).
30. B. A. Franz, E. J. Ainsworth, and S. Bailey, "SeaWiFS vicarious calibration: an alternative approach using in situ observations of oceanic and atmospheric optical properties," in *In Situ Aerosol Optical Thickness Collected by the SIMBIOS Program (1997–2000): Protocols, Data QC, and Analysis*, G. S. Fargion, R. A. Barnes, and C. McClain, eds., NASA Tech. Memo. 209982 (NASA Goddard Space Flight Center, 2001), pp. 88–96.
31. M. Wang, K. D. Knobelspiesse, and C. R. McClain, "Study of the Sea-viewing Wide Field-of-view Sensor (SeaWiFS) aerosol optical property data over ocean in combination with the ocean color products," *J. Geophys. Res.* **110**, D10S06 (2005).
32. R. E. Eplee, Jr. and F. S. Patt, "Cloud-top radiance analysis for SeaWiFS bilinear knee calibration," in *SeaWiFS Postlaunch Calibration and Validation Analyses, Part 1*, S. B. Hooker and E. R. Firestone, eds. **9**, NASA Tech. Memo. 206892 (NASA Goddard Space Flight Center, 2000), pp. 13–16.
33. R. E. Eplee, Jr., S. W. Bailey, R. A. Barnes, H. H. Kieffer, and C. R. McClain, "Comparison of SeaWiFS on-orbit lunar and vicarious calibrations," *Proc. SPIE* **6296**, 629610 (2006).
34. B. C. Johnson, S. W. Brown, and H. W. Yoon, "Radiometric calibration history of visible and near-infrared portable radiometers," *Metrologia* **37**, 423–426 (2000).
35. C. R. McClain, "A decade of satellite ocean color observations," *Annu. Rev. Mar. Sci.* **1**, 19–42 (2009).
36. T. S. Kostadinov, D. A. Siegel, and S. Maritorena, "Global phytoplankton functional types from space: assessment vis the particle size distribution," *Biogeosciences* **7**, 3239–3257 (2010).
37. S. A. Henson, J. L. Sarmiento, J. P. Dunne, L. Bopp, I. Lima, S. C. Doney, J. John, and C. Beaulieu, "Detection of anthropogenic climate change in satellite records of ocean chlorophyll and productivity," *Biogeosciences* **7**, 621–640 (2010).
38. F. P. Chavez, M. Messie, and J. T. Pennington, "Marine primary production in relation to climate variability and change," *Annu. Rev. Mar. Sci.* **3**, 227–260 (2011).
39. D. A. Siegel, M. J. Behrenfeld, S. Maritorena, C. R. McClain, D. Antoine, S. W. Bailey, P. S. Bontempi, E. S. Boss, H. M. Dierssen, S. C. Doney, R. E. Eplee, Jr., R. H. Evans, G. C. Feldman, E. Fields, B. A. Franz, N. A. Kuring, C. Mengelt, N. B. Nelson, F. S. Patt, W. D. Robinson, J. L. Sarmiento, C. M. Swan, P. J. Werdell, T. K. Westberry, J. G. Wilding, and J. A. Yoder, "Regional and global assessments of phytoplankton dynamics from the SeaWiFS mission," *Remote Sens. Environ.* (to be published, 2013).
40. C. Wilson, "The rocky road from research to operations for satellite ocean-colour data in fishery management," *ICES J. Mar. Sci.* **68**, 677–686 (2011).
41. R. P. Stumpf, M. E. Culver, P. A. Tester, M. Tomlinson, G. J. Kirkpatrick, B. A. Pederson, E. Truby, V. Ransibrahmanakul, and M. Soracco, "Monitoring *Karenia brevis* blooms in the Gulf of Mexico using satellite ocean color imagery and other data," *Harmful Algae* **2**, 147–160 (2003).
42. D. A. Siegel and B. A. Franz, "Century of phytoplankton change," *Nature* **466**, 569–571 (2010).
43. National Research Council, *From Research to Operations in Weather Satellites and Numerical Weather Prediction: Crossing the Valley of Death* (The National Academies, 2000).
44. National Research Council, *Satellite Observations of the Earth's Environment: Accelerating the Transition of Research to Operations* (The National Academies, 2003).
45. National Research Council, *Assessing Requirements for Sustained Ocean Color Research and Operations* (The National Academies, 2011).
46. R. E. Eplee, Jr., G. Meister, F. S. Patt, B. A. Franz, and C. R. McClain, "Uncertainty assessment of the SeaWiFS on-orbit calibration," *Proc. SPIE* **8153**, 81530B (2011).